

# GA-NIFS: Witnessing the complex assembly of a massive star-forming system at $z = 5.7$

Gareth C. Jones<sup>1\*</sup>, Andrew J. Bunker<sup>1</sup>, Kseniia Telikova<sup>2</sup>, Santiago Arribas<sup>3</sup>, Stefano Carniani<sup>4</sup>, Stephane Charlot<sup>5</sup>, Francesco D'Eugenio<sup>6,7</sup>, Roberto Maiolino<sup>6,7,8</sup>, Michele Perna<sup>3</sup>, Bruno Rodríguez Del Pino<sup>3</sup>, Hannah Übler<sup>6,7</sup>, Chris Willott<sup>9</sup>, Manuel Aravena<sup>2</sup>, Torsten Böker<sup>10</sup>, Giovanni Cresci<sup>11</sup>, Mirko Curti<sup>12</sup>, Rodrigo Herrera-Camus<sup>13</sup>, Isabella Lamperti<sup>3</sup>, Eleonora Parlanti<sup>4</sup>, Pablo G. Pérez-González<sup>3</sup>, Vicente Villanueva<sup>13</sup>

<sup>1</sup>Department of Physics, University of Oxford, Denys Wilkinson Building, Keble Road, Oxford OX1 3RH, UK

<sup>2</sup>Instituto de Estudios Astrofísicos, Facultad de Ingeniería y Ciencias, Universidad Diego Portales, Av. Ejército Libertador 441, 8370191 Santiago, Chile

<sup>3</sup>Centro de Astrobiología (CAB), CSIC-INTA, Cra. de Ajalvir Km. 4, 28850- Torrejón de Ardoz, Madrid, Spain

<sup>4</sup>Scuola Normale Superiore, Piazza dei Cavalieri 7, I-56126 Pisa, Italy

<sup>5</sup>Sorbonne Université, CNRS, UMR 7095, Institut d'Astrophysique de Paris, 98 bis bd Arago, 75014 Paris, France

<sup>6</sup>Kavli Institute for Cosmology, University of Cambridge, Madingley Road, Cambridge CB3 0HA, UK

<sup>7</sup>Cavendish Laboratory, University of Cambridge, 19 JJ Thomson Avenue, Cambridge CB3 0HE, UK

<sup>8</sup>Department of Physics and Astronomy, University College London, Gower Street, London WC1E 6BT, UK

<sup>9</sup>NRC Herzberg, 5071 West Saanich Rd, Victoria, BC V9E 2E7, Canada

<sup>10</sup>European Space Agency, c/o STScI, 3700 San Martin Drive, Baltimore, MD 21218, USA

<sup>11</sup>INAF - Osservatorio Astrofisico di Arcetri, largo E. Fermi 5, 50127 Firenze, Italy

<sup>12</sup>European Southern Observatory, Karl-Schwarzschild-Strasse 2, 85748 Garching, Germany

<sup>13</sup>Departamento de Astronomía, Universidad de Concepción, Barrio Universitario, Concepción, Chile

Accepted XXX. Received YYY; in original form ZZZ

## ABSTRACT

We present observations of the  $z \sim 5.7$  Lyman-break galaxy HZ10 with the JWST/NIRSpec IFU in high and low spectral resolution (G395H,  $R \sim 2700$  and PRISM,  $R \sim 100$ , respectively), as part of the GA-NIFS program. By spatially resolving the source, we find evidence for three spatially and spectrally distinct regions of line emission along with one region of strong continuum emission, all within a projected distance of  $< 10$  kpc. The R2700 data features strong detections in H $\beta$ , [OIII] $\lambda\lambda 4959, 5007$ , [NII] $\lambda\lambda 6548, 6584$ , H $\alpha$ , and [SII] $\lambda\lambda 6716, 6731$ . The R100 data additionally contains a strong detection of the Ly $\alpha$  break, rest-UV continuum, and [OII] $\lambda\lambda 3726, 3729$ . None of the detected lines present strong evidence for AGN excitation from line diagnostic diagrams, and no high-ionisation lines are detected. Using the detected lines, we constrain the electron density ( $\log_{10}(n_e/\text{cm}^{-3}) \sim 2.5 - 3.3$ ) and metallicity ( $\sim 0.5 - 0.7$  solar) in each component. Spaxel-by-spaxel fits of each cube reveal a strong east-west velocity gradient and significant line asymmetries (indicating tidal features or outflows). The western component features a very red UV slope ( $\beta_{UV} \sim -1$ ) and significant H $\alpha$  emission, suggesting an evolved population and active star formation. From a comparison to high resolution [C II] 158  $\mu\text{m}$  imaging obtained with the Atacama Large Millimetre/submillimetre Array (ALMA), we find that the continuum emitter is associated with a gas-poor stellar population. Altogether, these data suggest that HZ10 represents an ongoing merger, with a complex distribution of stars, gas, and dust  $< 1$  Gyr after the Big Bang.

**Key words:** galaxies: high-redshift - galaxies: interactions - galaxies: kinematics and dynamics - galaxies: ISM

## 1 INTRODUCTION

Studies of local galaxies have shown that the majority of them are relaxed disks with spiral arms (e.g., Delgado-Serrano et al. 2010). But when the Universe was much younger ( $\lesssim 1.5$  Gyr after the Big Bang,  $z > 4$ ), this was not the case. In the early Universe, observational studies have found that the fraction of galaxies with spiral features decreases with increasing redshift (Kuhn et al. 2023), while the major

merger fraction increases with redshift (e.g., Rodrigues et al. 2017; Duncan et al. 2019; Ferreira et al. 2020). A survey of  $z \sim 4 - 6$  galaxies with the Atacama Large Millimetre/submillimetre Array (ALMA) revealed a small fraction of rotating disks, with a high number of mergers (e.g., Le Fèvre et al. 2020; Jones et al. 2021; Romano et al. 2021; The ALMA Large Program to Investigate [C II] at Early Times; ALPINE). This agrees with the results of cosmological zoom-in simulations of high-redshift galaxies, which show that the evolution of these sources is heavily influenced by frequent major

\* E-mail: gareth.jones@physics.ox.ac.uk

and minor mergers (e.g., Pallottini et al. 2017; Kohandel et al. 2019; Kretschmer et al. 2022).

Since the secure identification of merging activity requires resolved observations of galaxy kinematics (e.g., Simons et al. 2019), much progress has been made by observing the strong far-infrared (FIR) emission line [C II] 158  $\mu\text{m}$  (hereafter [C II]). In general, [C II] observations of  $z > 4$  galaxies tend to show multiple star-forming clumps or extensions (e.g., Carilli et al. 2013; Bischetti et al. 2018; Carniani et al. 2018; Le Fèvre et al. 2020; Nguyen et al. 2020). Some high spatial resolution ( $\sim 1 - 3$  kpc) [C II] observations of these galaxies reveal the presence of ordered rotation (e.g., Neeleman et al. 2020; Rizzo et al. 2020; Fraternali et al. 2021; Lelli et al. 2021; Herrera-Camus et al. 2022; Posses et al. 2023; Roman-Oliveira et al. 2023), but often with nearby companions or departures from regular rotation that could indicate the influence of a nearby merging companion galaxy.

While these ALMA observations are powerful tools for determining the morpho-kinematics of the cold interstellar medium (ISM) in these galaxies, they may only be used to estimate dust properties (from the FIR spectral energy distribution; SED), dynamical mass, and either the molecular gas mass (e.g., Zanella et al. 2018; Vizgan et al. 2022a) or star formation rate (SFR; e.g., De Looze et al. 2014; Schaefer et al. 2020). For a more complete census of the ISM and galaxy properties in the context of their morpho-kinematics (including the existence of feedback; e.g., Perna et al. 2020; Fluetsch et al. 2021; Cresci et al. 2023), observations of ionised lines in the rest-optical are required. With the advent of the JWST and the integral field unit (IFU; Böker et al. 2022) on the Near Infrared Spectrograph (NIRSpec; Jakobsen et al. 2022), we may now conduct spatially resolved observations of high-redshift galaxies in rest-UV and rest-optical continuum emission and emission lines, shedding light on stellar populations and the ISM.

The NIRSpec IFU has been used to characterise the morpho-kinematics and ISM conditions for multiple  $z > 4$  galaxies (e.g., Hashimoto et al. 2023; Loiacono et al. 2024; Venturi et al. 2024), with a large portion of the observations originating from the Galaxy Assembly with NIRSpec Integral Field Spectroscopy (GA-NIFS) Guaranteed Time Observations (GTO) program (PIs: R. Maiolino & S. Arribas; Arribas et al. 2023; Marshall et al. 2023; Übler et al. 2023, 2024a,b; Ji et al. 2024; Jones et al. 2024a; Parlanti et al. 2024). This program contains observations of 55 diverse galaxies (e.g., quasar host galaxies, star-forming galaxies, rotators, mergers) between  $z \sim 2 - 11$  with the NIRSpec IFU (see also D’Eugenio et al. 2023a; Perna et al. 2023a,b; Pérez-González et al. 2024; Rodríguez Del Pino et al. 2024). In this work, we analyse data from GA-NIFS observations of the galaxy HZ10 at  $z \sim 5.7$ .

HZ10 was originally detected as a Lyman break galaxy (LBG) in the 2 square degree Cosmic Evolution Survey (COSMOS; Scoville et al. 2007) field. Photometric observations with Subaru/Suprime-Cam revealed evidence for significant Ly $\alpha$  emission at  $z \sim 5.7$  (observed-frame equivalent width of  $75 \pm 22\text{\AA}$ ; source 66 of Murayama et al. 2007). Followup observations with the Deep Extragalactic Imaging Multi-Object Spectrograph (DEIMOS) on the W. M. Keck-II Observatory revealed that this source is a UV-luminous ( $M_{UV} = -22.56 \pm 0.15$ ) Ly $\alpha$  emitter at  $z_{sys} = 5.659$ , with a red UV slope ( $\beta_{UV} < -0.6$ ) and a large stellar mass ( $\log_{10}(M_*/M_\odot) = 10.39 \pm 0.17$ ; Capak et al. 2015). It was selected as one of the first high-redshift objects to be observed in [C II] emission with ALMA (project 2012.1.00523.S, PI P. Capak).

In the sample of ten  $z \sim 5.1 - 5.7$  LBGs in Capak et al. (2015), HZ10 was the brightest ( $S_{158\mu\text{m}} = 1.261 \pm 0.044$  mJy) and largest (beam-deconvolved FWHM of  $(1.16 \pm 0.11)'' \times (0.59 \pm 0.03)''$  at

$83.2 \pm 3.1^\circ$ ) FIR continuum source. Based on this detection and assuming a modified blackbody model, Capak et al. estimate an infrared luminosity  $\log_{10}(L_{IR}/L_\odot) = 11.94 \pm 0.08$  and  $\text{SFR}_{IR} = 169^{+32}_{-27} M_\odot \text{ year}^{-1}$ . Both the [C II] and FIR continuum emission of HZ10 feature an east-west elongation, where the eastern end overlaps with UV emission (Subaru  $z'$  band).

Further analysis of the [C II] data by Pavese et al. (2016) returned a precise  $z_{[CII]} = 5.6543 \pm 0.0003$ ,  $\log_{10}(L_{[CII]}/L_\odot) = 9.60 \pm 0.03$ , and the detection of a velocity gradient ( $\text{FWHM} \sim 630 \text{ km s}^{-1}$ ). While [NII] 205  $\mu\text{m}$  was significantly detected ( $> 3\sigma$ ), it featured a smaller full width at half maximum (FWHM), was redshifted, and spatially extended to the west. Based on the observed properties, Pavese et al. suggest that HZ10 may represent an ongoing major merger. Kinematic modelling of the [C II] data cube (Pavese et al. 2019) resulted in a dynamical mass estimate of  $\log_{10}(M_{dyn}/M_\odot) = 10.79 \pm 0.05$ , in agreement with other analyses (Capak et al. 2015; Jones et al. 2017).

This source has also been detected in CO(2-1) emission (Pavese et al. 2019), where an assumed conversion factor of  $\alpha_{CO} = 4.5 M_\odot \text{ K}^{-1} \text{ km}^{-1} \text{ pc}^{-2}$  yielded a molecular gas mass of  $\log_{10}(M_{gas}/M_\odot) = 11.1 \pm 0.1$ . Followup observations of CO(5-4) and CO(6-5) (Vieira et al. 2022) did not recover significant emission. A detection of CIII] $\lambda 1909$  enabled Markov et al. (2022) to estimate the gas-phase metallicity of HZ10 ( $Z = 0.60^{+0.32}_{-0.52} Z_\odot$ ).

A massive starburst galaxy (CRLE,  $z = 5.667$ ) nearby to HZ10 ( $13'' \sim 77$  kpc in projected distance;  $\Delta v \sim 580 \text{ km s}^{-1}$ ) was serendipitously detected through [C II], [NII]205  $\mu\text{m}$ , and CO(2-1) observations (Pavese et al. 2018). A further search of the COSMOS2015 photometric redshift catalogue (Laigle et al. 2016) revealed the presence of a galaxy overdensity (eight galaxies within  $3'$  of CRLE), which may be an early protocluster.

Altogether, these previous findings present a complex picture of HZ10. It is gas-rich, dynamically massive, and FIR bright. But its asymmetric velocity field and frequent spatial shift between tracers (e.g., [C II] and [NII]) argue against a single source. One possible route towards determining the nature of this galaxy is to examine the rest-frame optical properties of this object on a resolved scale, but this was not previously possible.

In this work we present new JWST/NIRSpec IFU observations of HZ10 to further investigate this well-studied, but still mysterious system. The details of our observations and calibration procedure are given in Section 2. These data are analysed in Section 3, and we discuss the results in Section 4. We conclude in Section 5. We assume a standard concordance cosmology ( $\Omega_\Lambda, \Omega_m, h$ ) = (0.7, 0.3, 0.7) throughout. At the approximate redshift of this source ( $z = 5.6543$ ),  $1''$  corresponds to 5.90 projected kpc. Emission lines are named based on their air wavelength, while we use their vacuum wavelengths for analysis (e.g.  $\lambda_{[OIII]\lambda 5007} = 5008.24\text{\AA}$ ).

## 2 OBSERVATIONS AND CALIBRATION

The data analysed here originated from GA-NIFS observations as part of project 1217 (PI: N. Luetzgendorf; details in Table 1). An eight-point ‘MEDIUM’ dither pattern was used, with a starting point of ‘1’. Data were taken at both low (PRISM/CLEAR;  $R \sim 100$ , hereafter R100) and high spectral resolution (G395H/F290LP;  $R \sim 2700$ , hereafter R2700). The data were calibrated with the STScI pipeline (v11.1, CRDS 1149), with custom outlier rejection (D’Eugenio et al. 2023a), custom masks for cosmic ray strikes (‘snowballs’) or open MSA shutters,  $1/f$  noise corrections for count-rate maps, and drizzle

**Table 1.** JWST NIRSpec/IFU observation properties.

Grating/Filter	G395H/290LP	PRISM/CLEAR
Readout Pattern	NRSIRS2	NRSIRS2RAPID
Groups/Int	31	33
Ints/Exp	1	1
Exposures	8	8
Total Time [s]	18206.935	3968.178

weighting to create data cubes with spatial pixels (spaxels) of width  $0.05''$  (see Perna et al. 2023a for full details of reduction).

To verify the astrometry of our data, we first downloaded HST/WFC3 images from the Mikulski Archive for Space Telescopes (MAST<sup>1</sup>) archive (F125W, F160W, F105W). These images have been aligned to the *Gaia* DR3 reference frame (Gaia Collaboration et al. 2016, 2021), and are well-suited for astrometric comparison. Comparison images were created by convolving the R100 data cube with each HST/WFC3 filter bandpass function. No significant offset (i.e.,  $> 0.1''$ ) between the HST and JWST images was found, so no astrometric correction was performed. We have also confirmed that the R100 and R2700 cubes are aligned to the same frame (see Appendix A).

No background exposures were included in these observations, so we manually performed a background subtraction for each cube (R100 and R2700) by extracting a mean spectrum from a large, signal-free area in the cube. This mean background spectrum was then subtracted from each spaxel.

### 3 ANALYSIS

#### 3.1 Overview of continuum and line emission

An initial investigation of the IFU data cubes revealed that HZ10 is composed of multiple regions of strong emission. To illustrate this, we compare the  $\lambda_{obs} = 4 \mu\text{m}$  continuum (stellar emission redward of the Balmer break) and [OIII] $\lambda 5007$  emission from our R2700 data in Figure 1 (full details of this fit are presented in Section 3.3.1). It is clear that the line emission is concentrated in three components (here called HZ10-E, HZ10-C, and HZ10-W), while the rest-optical continuum is located at the position of HZ10-W and to the north of HZ10-E and HZ10-C.

Our ability to detect individual regions is partly due to the narrow point spread function (PSF) of our data ( $< 0.2''$ ) compared to previous ALMA observations ( $> 0.6''$ ; Capak et al. 2015). HZ10-E and HZ10-C are only separated by a projected distance of  $\sim 0.27''$  ( $\sim 1.6 \text{ kpc}$ ), so previous observations lacked the resolution to separate them (although see novel high-resolution ALMA [C II] observations of HZ10; Telikova et al. in prep, Villanueva et al. in prep).

We characterise the emission in this field using two primary methods. First, we analyse emission from the line peaks (see white circles in Figure 1; Section 3.2). Next, in Section 3.3 we take advantage of our high spatial resolution by performing spaxel-by-spaxel fits to each data cube. In addition to these analyses, we examine the full field by extracting integrated spectra using the large dashed white ellipsoidal aperture of Figure 1 (Appendix B).

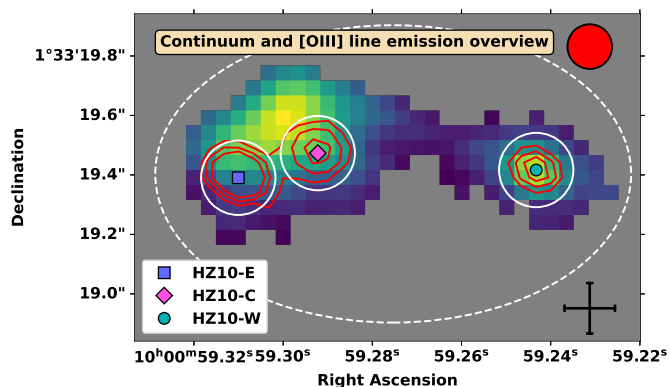


**Figure 1.** Demonstration of how emission in the HZ10 field is distributed. The colour shows the  $\lambda_{obs} = 4 \mu\text{m}$  continuum level as derived from spaxel-by-spaxel fits to the R2700 data cube (see Section 3.3.1). The distribution of [OIII] $\lambda 5007$  emission (from the same fits) is presented with red contours. The line emission is concentrated in three regions, which we denote as HZ10-E, HZ10-C, and HZ10-W (increasing in redshift and moving from east to west). The apertures we use to extract spectra of each component (Section 3.2) are shown as white circles. A large white dashed ellipse marks the extraction aperture for the analysis of Appendix B. The fiducial PSF of the data (FWHM= $0.15''$ ) is shown by a red ellipse to the upper right. A scale of 1 kpc (at a systemic redshift of  $z = 5.6543$ ) is shown by a black cross to the lower right. North is up and east is to the left.

#### 3.2 Component Analysis

We begin by extracting integrated spectra from the R100 and R2700 cubes using circular apertures (radius  $0.125''$ ) centred on the line peaks of each component (white circles in Figure 1) and fitting the line and continuum emission. We include H $\beta$ , [OIII] $\lambda 4959$ , [OIII] $\lambda 5007$ , [NII] $\lambda 6548$ , H $\alpha$ , [NII] $\lambda 6584$ , [SII] $\lambda 6716$ , and [SII] $\lambda 6731$  in the R2700 fit, while the wider spectral coverage of the R100 data ( $\sim 0.6 - 5.2 \mu\text{m}$ ) allows us to also fit [OII] $\lambda \lambda 3726, 3729$ . A corrected error spectrum is derived by rescaling the pipeline-output error array to match the standard deviation of sigma-clipped data (e.g., Übler et al. 2024b; Jones et al. 2024a). For R100, we derive the scaling factor using data in a spectrally flat region ( $\sim 4 \mu\text{m}$ ).

We adopt the standard assumptions of [NII] $\lambda 6584$ /[NII] $\lambda 6548 = 2.94$  (e.g. Dojčinović et al. 2023) and [OIII] $\lambda 5007$ /[OIII] $\lambda 4959 = 2.98$  (e.g. Dimitrijević et al. 2007) for each fit. The ratio [SII] $\lambda 6716$ /[SII] $\lambda 6731$  is a strong tracer of electron density, and is restricted to a range of  $\sim 0.55 - 1.45$ , assuming  $T_e = 10^4 \text{ K}$  (e.g., Le Tiran et al. 2011; Della Bruna et al. 2020). Due to the low spectral resolution, we model [OII] $\lambda \lambda 3726, 3729$  as a single Gaussian.

The line widths of the R100 fits are set using the fiducial line spread function (LSF<sup>2</sup>; i.e., each line is assumed to be unresolved in velocity space). Previous investigations using the micro-shutter assembly (MSA) on NIRSpec have found that the true LSF is narrower than the fiducial profile (e.g., de Graaff et al. 2024; Jones et al. 2024a). This is due to the fact that the fiducial spectral resolving power curve was derived assuming a uniformly lit MSA slit (width  $0.2''$ ), while many targets did not fill the slit. However, the IFU constructs data cubes using an image slicer with a narrower width ( $0.1''$ ), so the fiducial LSF should be appropriate for our analysis. Regardless, the

<sup>1</sup> <https://mast.stsci.edu/portal/Mashup/Clients/Mast/Portal.html>

<sup>2</sup> As recorded in the JWST documentation; <https://jwst-docs.stsci.edu/jwst-near-infrared-spectrograph/nirspec-instrumentation/nirspec-dispersers-and-filters>



LSF-deconvolved width of the R100 lines is not used in this work. Future works will investigate the LSF of the IFU in more detail.

For the R2700 spectra, we allow each line to contain a narrow and broad model component at different velocities ( $z_1$  for the narrower component, and  $z_2$  for the broader component), resulting in low residuals. This represents a two-zone model, where the narrow emission originates from core galaxies and the broad component may originate from nearby tidal features or outflows. This assumption is inspected further in Section 3.3.1 and Appendix C.

To allow for the suppression of [OIII] $\lambda\lambda$ 4959,5007 and other forbidden lines in high-density environments (see Section 4.1.1), we separate the FWHM values of the Balmer lines ( $H\alpha$  and  $H\beta$ ) from the other lines. That is, we fit for four FWHM values (in  $\text{km s}^{-1}$ ) for each extracted spectrum: the narrow and broad FWHMs for the Balmer lines, and the narrow and broad FWHMs for the other lines. We account for the effect of the spectral resolving power on each linewidth when calculating each FWHM in the R2700 spectrum.

The continuum of the R2700 spectrum is taken into account by including a single power law in the model. For the R100 spectrum, the  $\text{Ly}\alpha$  break was modelled using a Heaviside function. To allow for a discontinuity around the Balmer break, we fit the continuum redwards and bluewards of a Balmer series line ( $H\eta$ ) with separate power law models. Previous studies have found that the continuum redwards of the  $\text{Ly}\alpha$  break may deviate from the single power law seen at rest-UV wavelengths (e.g., Cameron et al. 2023a; Jones et al. 2024b). This effect is accounted for by fitting the continuum red- and blue-wards of a pivot wavelength ( $\lambda_{rest} = 0.15 \mu\text{m}$ ) with separate power law components, with the same value at their overlapping wavelength. Due to the low spectral resolution of these data, we convolve the continuum model with a wavelength-dependent Gaussian representing the LSF (e.g., Jones et al. 2024a; Umeda et al. 2023; Heintz et al. 2023; Napolitano et al. 2024).

Each spectrum is fit with LMFIT (Newville et al. 2014) in ‘least\_squares’ mode, using inverse variance weighting. The resulting best-fit models are shown in Figure 2 for R2700 data and Figure 3 for R100 data. The best-fit parameters are presented in Table 2.

### 3.2.1 Results

The spectra of all three components are well-fit with our models, resulting in low residuals and estimates of redshift, UV magnitude, UV spectral slope, line-width, and line fluxes.

We are able to measure  $z_{sys}$  from the R100 spectra, as well as the redshifts of the narrow ( $z_{sys,N}$ ) and broad contributions ( $z_{sys,B}$ ) in the R2700 spectra. For all components, the R100-based redshift is  $> 3\sigma$  higher than either of the R2700-based redshifts. To explain this, we note that recent NIRSpec studies using the MSA (e.g., D’Eugenio et al. 2024) have found a spectral offset between R100 and R2700 data due to NIRSpec wavelength calibration issues. Since this affects all NIRSpec observations, IFU data may be affected as well, as confirmed by Pérez-González et al. (2024). These authors prefer the R2700 redshift over the R100 redshift, based on the fact that the R2700 redshift is in better agreement with the ALMA-based redshift.

Taking the [C II] redshift of Pavesi et al. (2016) as the systemic redshift, we see that both HZ10-E and HZ10-C feature blueshifted narrow emission with broad emission that is relatively redshifted. The inverse is true for HZ10-W. The total velocity difference between the narrow components of HZ10-E and HZ10-W is large ( $\sim 740 \text{ km s}^{-1}$ ), but the difference between the other component pairs is  $< 500 \text{ km s}^{-1}$ .

None of the R100 spectra show evidence for significant  $\text{Ly}\alpha$  emission. Since the previously reported detection of  $\text{Ly}\alpha$  in HZ10 (Mu-

rayama et al. 2007) used a larger aperture, we also search for  $\text{Ly}\alpha$  using the dashed ellipse in Figure 1 (see analysis of Section B). Even with a broader aperture, we do not detect  $\text{Ly}\alpha$ . However, our  $3\sigma$  upper limit on the rest-frame equivalent width of  $\text{Ly}\alpha$  is in agreement with that of Murayama et al. (2007), suggesting that higher sensitivity observations are required.

Of the three components, HZ10-C is the most UV-bright ( $M_{UV} = -20.67 \pm 0.01$ ) and features the bluest continuum slope ( $\beta_{UV} = -1.99 \pm 0.01$ ). On the other hand, HZ10-W is the most UV-faint ( $M_{UV} = -19.4 \pm 0.04$ ) and features the reddest continuum slope ( $\beta_{UV} = -1.04 \pm 0.03$ ), and HZ10-E is intermediate in both measures. This is discussed further in Section 4.3.

### 3.2.2 Line ratio analysis

Using the line fluxes from the spectral analysis detailed in the previous subsection, we next explore the position of these components on line ratio diagrams (see Table 3 for definitions of ratios used in this work). These include the [NII]-BPT ( $\log_{10}R3$  vs  $\log_{10}N2$ ; Baldwin et al. 1981) and [SII]-VO87 ( $\log_{10}R3$  vs  $\log_{10}S2$ ; Veilleux & Osterbrock 1987) diagrams. Historically, these plots have been used to determine if galaxies are primarily powered by star formation (low N2, R3, and S2), AGN (high N2, R3, and S2), or a composite of the two (intermediate N2 and R3; e.g., Ibar et al. 2015; Mazzilli Ciraulo et al. 2021; Richings et al. 2021). While the standard demarcation lines (Kewley et al. 2001; Kauffmann et al. 2003b) are suitable for high-metallicity, massive systems, they were derived for low-redshift galaxies. Some models and observations suggest that these criteria are not suitable for low-metallicity sources at high-redshift ( $z > 4$ ; e.g., Feltre et al. 2016; Nakajima & Maiolino 2022; Maiolino et al. 2023; Übler et al. 2023; Dors et al. 2024). Indeed, the location of galaxies on these diagrams is affected by a number of parameters (e.g.,  $Z$ , presence of shocks, ionisation parameter, hydrogen density; Allen et al. 2008; Feltre et al. 2016; Sugahara et al. 2021), so additional diagnostics are required for concrete conclusions. In this work, we utilise the demarcation lines of Scholtz et al. (2023), which were derived from JWST/NIRSpec observations to separate extreme AGN (above each line) from all other sources at high redshift (including both weaker AGN and SFGs; below each line).

The resulting diagnostic plots are presented in Figure 4. Due to the construction of our models, we may examine the flux ratios of the best-fit narrow (blue outlined symbols), broad (red outlined symbols), and total model (black outlined symbols) for each component. Using the best-fit line fluxes from fits of the R2700 data, we find that the components of HZ10 feature similar line ratios to other observed  $z = 5.5 - 7.0$  galaxies (Cameron et al. 2023b; Jones et al. 2024a). All components fall underneath the Scholtz et al. (2023) line for the [NII]-BPT diagram, but both of the total best-fit models for HZ10-E and HZ10-W lie on the demarcation line for the [SII]-VO87 relation. The broad components and upper limits on the narrow components of HZ10-C and HZ10-E lie above the [SII]-VO87 relation demarcation line, adding slight evidence for the presence of an AGN. Because none of the components lie far above the demarcation lines in both plots, there is no strong evidence for the presence of an AGN, although AGN contribution cannot be ruled out (see Section 4.1).

The observed line ratios may be used to determine the dust-corrected  $\text{SFR}_{H\alpha}$ . We first calculate the B-V colour excess from the Balmer decrement (e.g. Domínguez et al. 2013; Jones et al. 2024a). Combined with an assumed intrinsic value of  $F_{H\alpha}/F_{H\beta} = 2.86$  (Osterbrock 1989), we correct the observed  $F_{H\alpha}$  for dust obscuration and use the Kennicutt (1998) scaling law to predict the dust-corrected  $\text{SFR}_{H\alpha}$  (see Table 4). This sum of these  $\text{SFR}_{H\alpha}$  values over all three

**Table 2.** Best-fit line properties for HZ10, derived through separate fits to spectra extracted from  $r = 0.125''$  circular apertures centred on each component (see Figures 2 and 3). Results are listed for the R100 (first set of rows) and R2700 spectra (second set of rows) using multi-Gaussian and continuum models. FWHM values are given in  $\text{km s}^{-1}$ , while integrated fluxes are in  $10^{-20} \text{erg s}^{-1} \text{cm}^{-2}$ . The R100-based  $z_{\text{sys}}$  value is not used. Velocity offsets are given with respect to  $z_{[\text{C II}]} = 5.6543$  (Pavesi et al. 2016). For each line, we present the fluxes of the best-fit narrow component (N), broad component (B), and total model. Output uncertainties are given as  $1\sigma$ , and upper limits are given at  $3\sigma$ .

	HZ10-E	HZ10-C	HZ10-W
$z_{\text{sys}}$	$5.6528 \pm 0.0007$	$5.6593 \pm 0.0006$	$5.6646 \pm 0.0006$
$M_{UV}$	$-20.02 \pm 0.03$	$-20.67 \pm 0.01$	$-19.4 \pm 0.04$
$\beta_{UV}$	$-1.74 \pm 0.02$	$-1.99 \pm 0.01$	$-1.04 \pm 0.03$
$I_{[\text{O II}]\lambda\lambda 3726, 3729}$	$248 \pm 22$	$286 \pm 20$	$147 \pm 22$
$z_{\text{sys},N}$	$5.6436 \pm 0.0001$	$5.6524 \pm 0.0001$	$5.6601 \pm 0.0001$
$z_{\text{sys},B}$	$5.6485 \pm 0.0001$	$5.6537 \pm 0.0001$	$5.6569 \pm 0.0001$
$v_{\text{sys},N}$	$-480 \pm 13$	$-84 \pm 13$	$262 \pm 13$
$v_{\text{sys},B}$	$-262 \pm 17$	$-25 \pm 14$	$116 \pm 19$
$FWHM_{\text{Balmer},N}$	$140 \pm 6$	$151 \pm 12$	$241 \pm 10$
$FWHM_{\text{Balmer},B}$	$525 \pm 18$	$504 \pm 14$	$762 \pm 26$
$FWHM_{[\text{O III}],N}$	$130 \pm 4$	$108 \pm 13$	$239 \pm 13$
$FWHM_{[\text{O III}],B}$	$653 \pm 31$	$507 \pm 18$	$647 \pm 30$
$I_{H\beta,N}$	$42 \pm 3$	$41 \pm 5$	$51 \pm 5$
$I_{H\beta,B}$	$52 \pm 5$	$54 \pm 8$	$60 \pm 7$
$I_{H\beta}$	$94 \pm 6$	$95 \pm 9$	$111 \pm 9$
$I_{[\text{O III}]\lambda 4959,N}$	$84 \pm 2$	$36 \pm 3$	$40 \pm 3$
$I_{[\text{O III}]\lambda 4959,B}$	$46 \pm 3$	$66 \pm 3$	$46 \pm 3$
$I_{[\text{O III}]\lambda 4959}$	$130 \pm 4$	$102 \pm 4$	$86 \pm 4$
$I_{[\text{O III}]\lambda 5007,N}$	$250 \pm 5$	$106 \pm 8$	$121 \pm 9$
$I_{[\text{O III}]\lambda 5007,B}$	$138 \pm 10$	$198 \pm 10$	$137 \pm 10$
$I_{[\text{O III}]\lambda 5007}$	$389 \pm 11$	$304 \pm 13$	$258 \pm 13$
$I_{[\text{N II}]\lambda 6548,N}$	$3 \pm 1$	$3 \pm 1$	$33 \pm 2$
$I_{[\text{N II}]\lambda 6548,B}$	$24 \pm 2$	$41 \pm 2$	$48 \pm 4$
$I_{[\text{N II}]\lambda 6548}$	$28 \pm 3$	$44 \pm 2$	$82 \pm 4$
$I_{H\alpha,N}$	$161 \pm 7$	$114 \pm 10$	$235 \pm 13$
$I_{H\alpha,B}$	$214 \pm 10$	$309 \pm 10$	$358 \pm 17$
$I_{H\alpha}$	$375 \pm 12$	$423 \pm 14$	$593 \pm 21$
$I_{[\text{N II}]\lambda 6584,N}$	$9 \pm 4$	$9 \pm 3$	$98 \pm 7$
$I_{[\text{N II}]\lambda 6584,B}$	$71 \pm 7$	$121 \pm 6$	$142 \pm 10$
$I_{[\text{N II}]\lambda 6584}$	$81 \pm 8$	$130 \pm 7$	$240 \pm 12$
$I_{[\text{S II}]\lambda 6716,N}$	$< 37$	$< 36$	$23 \pm 6$
$I_{[\text{S II}]\lambda 6716,B}$	$43 \pm 6$	$64 \pm 5$	$26 \pm 9$
$I_{[\text{S II}]\lambda 6716}$	$43 \pm 6$	$64 \pm 5$	$49 \pm 11$
$I_{[\text{S II}]\lambda 6731,N}$	$7 \pm 3$	$< 29$	$27 \pm 5$
$I_{[\text{S II}]\lambda 6731,B}$	$38 \pm 8$	$56 \pm 5$	$< 33$
$I_{[\text{S II}]\lambda 6731}$	$45 \pm 9$	$56 \pm 5$	$27 \pm 5$

Ratio	Definition
R3	$[\text{O III}]\lambda 5007/H\beta$
N2	$[\text{N II}]\lambda 6584/H\alpha$
S2	$[\text{S II}]\lambda\lambda 6716, 6731/H\alpha$
RS32	$[\text{O III}]\lambda 5007/H\beta + [\text{S II}]\lambda\lambda 6716, 6731/H\alpha$
O3S2	$[\text{O III}]\lambda 5007/H\beta / [\text{S II}]\lambda\lambda 6716, 6731/H\alpha$
O3N2	$[\text{O III}]\lambda 5007/H\beta / [\text{N II}]\lambda 6584/H\alpha$

**Table 3.** Definitions of line flux ratios used in this work.

components ( $146 \pm 3 M_{\odot} \text{year}^{-1}$ ) contains contributions from both obscured and unobscured star formation activity, but it is lower than the obscured SFR of Capak et al. (2015):  $\text{SFR}_{\text{IR}} \sim 170 M_{\odot} \text{year}^{-1}$ . We note that these SFR tracers are also calibrated for different timescales, where  $\text{SFR}_{H\alpha}$  is associated with more recent SF (e.g., Kennicutt 1998). In addition, the Capak et al. (2015) SFR was derived using fits to a single FIR continuum point. Crucially, the  $H\alpha$ -based value presented here only represents emission from the three circular apertures in Figure 1, while Capak et al. (2015) integrate over the full field. Thus, it is likely that there is significant extended star

formation activity, as seen by the extension of line emission outside of the circular apertures in Figure 5.

We may use the  $[\text{S II}]\lambda 6716/[\text{S II}]\lambda 6731$  ratio of each component to constrain the electron density (Proxauf et al. 2014). While the resulting uncertainties are large, we find that the broad contributions of HZ10-E and HZ10-C feature higher densities ( $\sim 10^3 \text{cm}^{-3}$ ) than the narrow emission of HZ10-W ( $\sim 10^{2.5} \text{cm}^{-3}$ ). Previous studies of local galaxies found that broad, ionised outflows featured higher  $n_e$  than narrow host galaxies (e.g., Holt et al. 2011; Perna et al. 2017; Mingozzi et al. 2019), suggesting that the higher  $n_e$  in our broad component may originate from an outflow. The investigation of Davies et al. (2021) found a positive correlation between  $n_e$  and  $z$  for  $z < 2.6$  galaxies, which is likely caused by increased specific SFR ( $\text{sSFR} \equiv \text{SFR}/M_*$ ) at high redshift (i.e., the evolving normalisation of the star-forming main sequence; e.g., Speagle et al. 2014; Popesso et al. 2023). The  $n_e$  value of the narrow emission in HZ10-W is comparable to those of other  $z \sim 4 - 6$  galaxies (e.g., Isobe et al. 2023), in agreement with this trend.

Our dust-corrected line ratios (see Table 3) are combined with the metallicity diagnostics of Curti et al. (2020) to determine the

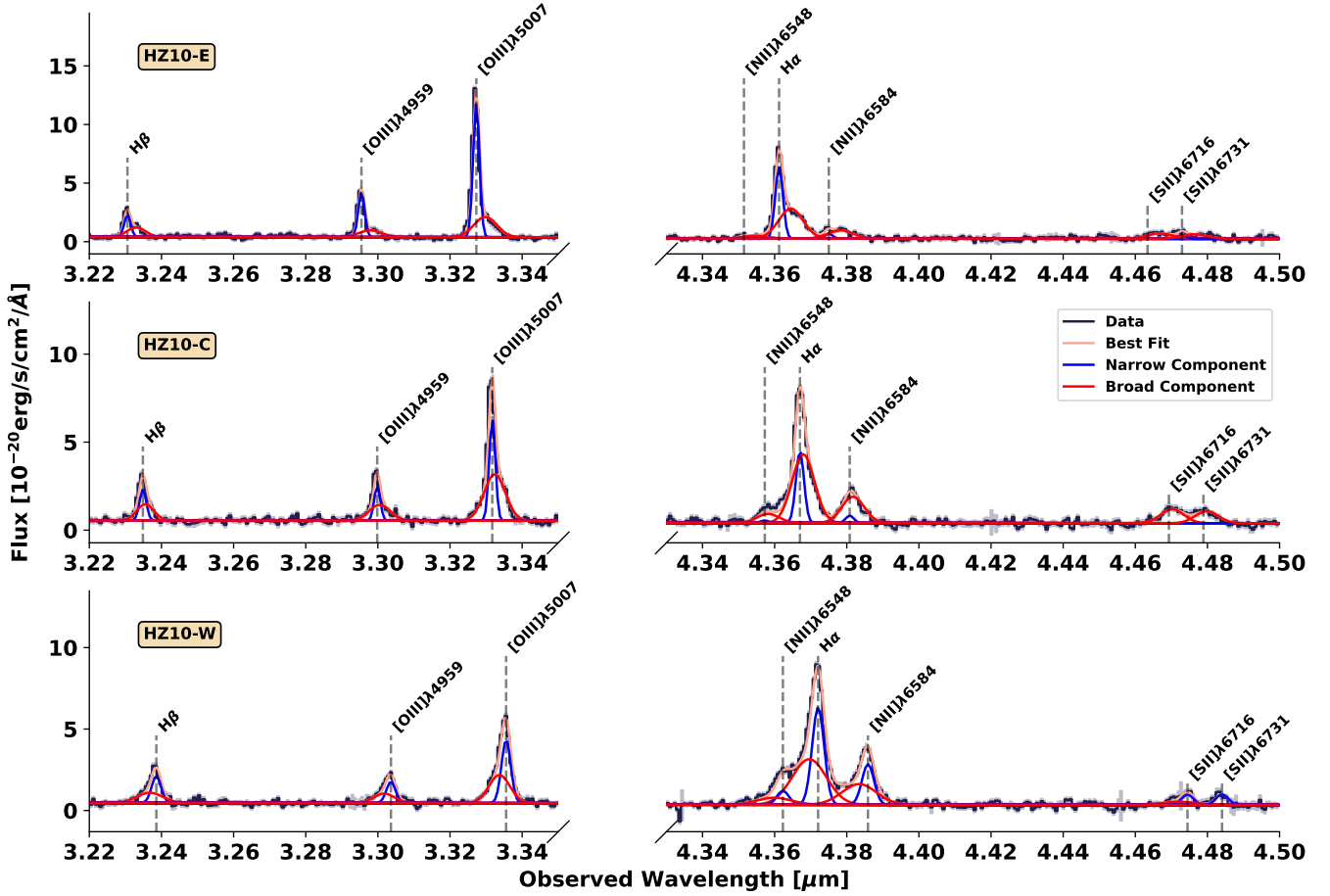


**Figure 2.** Spectra extracted from R2700 data cube using the circular apertures of Figure 1 for each component, as well as the best-fit full models, broad, and narrow contributions. We only show the wavelength range around studied emission lines.

gas-phase metallicity of each component. Note that we only include line fluxes determined from the R2700 data (i.e., excluding  $[\text{OII}]\lambda\lambda 3726, 3729$ ), as the complex line shapes and spectral blending cause R100-based line fluxes to be incorrectly estimated. Assuming a solar metallicity of  $8.69 \pm 0.05$  (Asplund et al. 2009), we find gas-phase metallicities of  $\sim 0.53 - 0.72$  solar for the three components (in agreement with Markov et al. 2022). These are higher than most galaxies in this epoch (e.g., Curti et al. 2024), but comparable to the metallicities found in other high-redshift merging systems (e.g., Arribas et al. 2023; Rodríguez Del Pino et al. 2024; Pérez-González et al. 2024; Venturi et al. 2024).

### 3.3 Spatially resolved analyses

While the component-based analysis allows us to characterise the three primary line-emitting regions and constrain some physical parameters, the nature of the NIRSPEC IFU also allows us to explore these properties in a resolved manner. That is, we may extract spectra from each spaxel of the R100 and R2700 cubes and fit each to reveal the ionised gas kinematics, metallicity, and morphology of the complex source HZ10.

	HZ10-E	HZ10-C	HZ10-W
$E(B-V)_N$	0.25	0	0.41
$E(B-V)_B$	0.31	0.59	0.63
$E(B-V)$	0.28	0.38	0.53
$\text{SFR}_{\text{H}\alpha, \text{DC}, \text{N}} [\text{M}_{\odot} \text{ year}^{-1}]$	$10 \pm 1$	$3 \pm 1$	$23 \pm 1$
$\text{SFR}_{\text{H}\alpha, \text{DC}, \text{B}} [\text{M}_{\odot} \text{ year}^{-1}]$	$15 \pm 1$	$52 \pm 2$	$68 \pm 3$
$\text{SFR}_{\text{H}\alpha, \text{DC}} [\text{M}_{\odot} \text{ year}^{-1}]$	$25 \pm 1$	$37 \pm 1$	$84 \pm 3$
$n_{\text{e}, \text{N}} [\text{cm}^{-3}]$	–	–	$2.51 \pm 0.01$
$n_{\text{e}, \text{B}} [\text{cm}^{-3}]$	$3.01 \pm 1.00$	$3.05 \pm 0.49$	–
$12 + \log_{10}(\text{O}/\text{H})_N$	$8.33 \pm 0.05$	$8.50 \pm 0.05$	$8.54 \pm 0.05$
$Z_N [Z_{\odot}]$	$0.43 \pm 0.07$	$0.65 \pm 0.11$	$0.71 \pm 0.12$
$12 + \log_{10}(\text{O}/\text{H})_B$	$8.53 \pm 0.05$	$8.54 \pm 0.05$	$8.55 \pm 0.05$
$Z_B [Z_{\odot}]$	$0.69 \pm 0.11$	$0.71 \pm 0.12$	$0.72 \pm 0.12$
$12 + \log_{10}(\text{O}/\text{H})$	$8.42 \pm 0.05$	$8.50 \pm 0.05$	$8.55 \pm 0.05$
$Z [Z_{\odot}]$	$0.53 \pm 0.09$	$0.64 \pm 0.11$	$0.72 \pm 0.12$

**Table 4.** Properties of HZ10 components derived from line ratio diagnostics. Included are the observed B-V colour excess derived from the Balmer decrement, the dust-corrected SFR derived from  $\text{H}\alpha$  intensity, the electron density derived from  $[\text{SII}]\lambda 6716/[\text{SII}]\lambda 6731$  ratios, and metallicities calculated using the diagnostics of Curti et al. (2020) and the line ratios listed in Table 3. We assume a Salpeter (1955) IMF and Calzetti et al. (2000) extinction law.

#### 3.3.1 R2700 resolved analysis

The R2700 data cube is a rich treasure trove of morpho-kinematic information, but the fact that the spectra of many spaxels exhibit

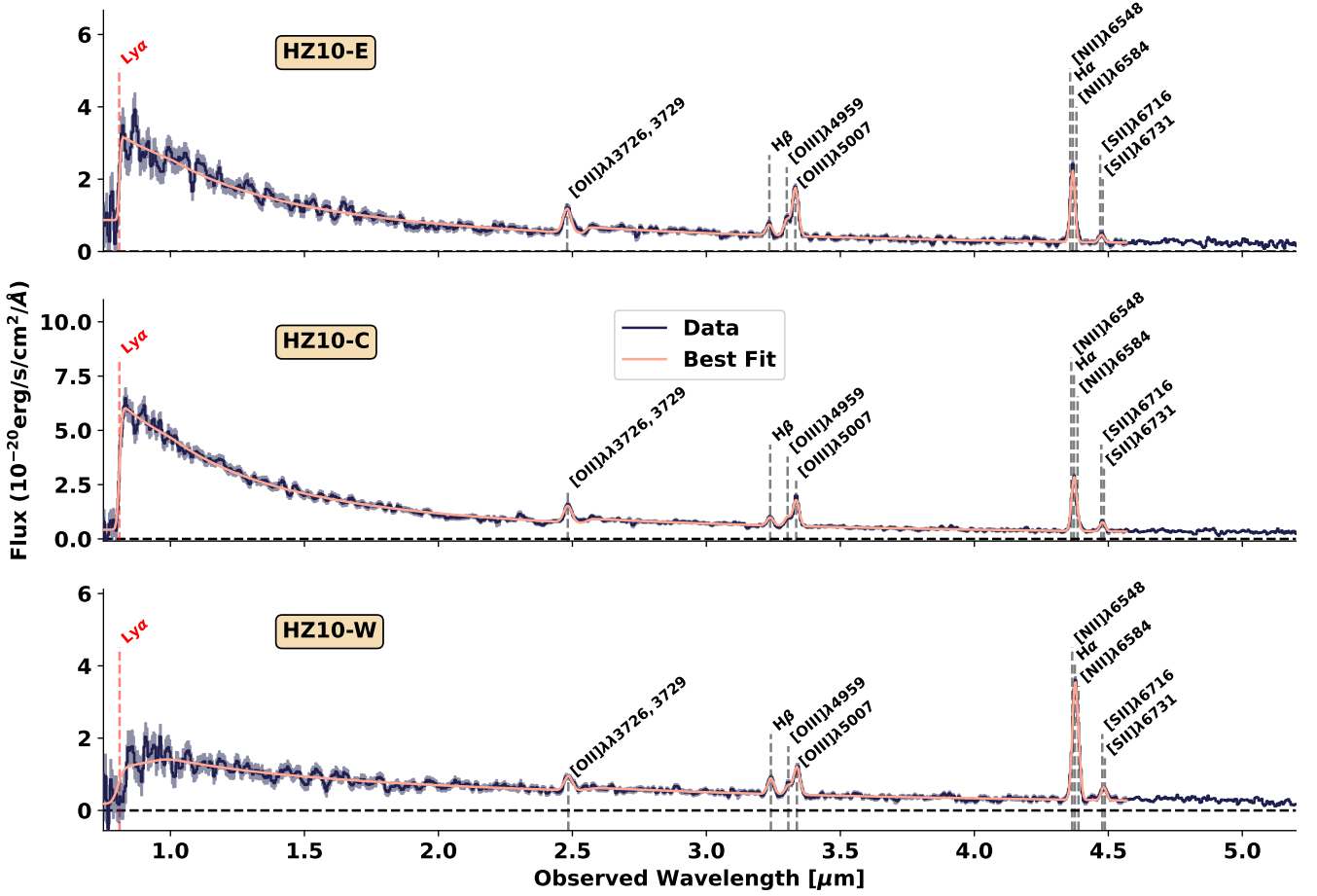


**Figure 3.** Spectra extracted from R100 data cube using the circular apertures of Figure 1 for each component, as well as the best-fit models. The expected wavelength of Ly $\alpha$  (which is not detected) is marked with a dashed red line.

non-symmetric emission lines complicates resolved analysis. These skewed lines could represent tidal interaction features or outflows (we examine evidence for the presence of a broad line region [BLR] in Section 4.1.1), as well as contamination from emission in other spaxels within the PSF. We explore the R2700 data cube by fitting the spectrum of each spaxel using the flexible line and continuum model detailed in Section 3.2.

The approach of fitting two components to each line (i.e., narrow and broad) is more suitable than a single-Gaussian approach, but may still simplify the distribution and source of flux in the HZ10 field. To test this, we performed a non-parametric kinematic analysis of the spectrally distinct [OIII] $\lambda$ 5007 emission (Appendix C). Since the results of the two-Gaussian and non-parametric approaches agree, the two-Gaussian approach is sufficient to capture the asymmetric morpho-kinematics of this field.

Using LMFIT in ‘least\_squares’ mode, we first fit each spectrum with all variables free. The results are inspected, and we fix the flux of all line components with  $S/N < 3$  to 0, and re-run the fit until only well-fit lines remain. Once the fit converges, we extract the continuum value, total line flux of each line, and velocity information from each best-fit model. The results are shown in Figure 5.

The fits are used to extract relevant kinematic measures for [OIII] $\lambda$ 5007 and H $\alpha$ . First, we consider  $v_X$ , or the velocity (with respect to a systemic redshift of  $z = 5.6534$ ) at which the cumulative distribution function (CDF) of the best-fit line model

(including both broad and narrow components) reaches a value of  $X\%$ . This results in estimates of  $v_{50}$ ,  $w_{80} \equiv v_{90} - v_{10}$ , and asymmetry =  $|v_{50} - v_{90}| - |v_{50} - v_{10}|$  (e.g., [Hervella Seoane et al. 2023](#)).

For each spaxel where H $\beta$ , [OIII] $\lambda$ 5007, [NII] $\lambda$ 6584, and H $\alpha$  are well detected, we apply the [NII]-BPT demarcation line of [Scholtz et al. \(2023\)](#) to test for extreme AGN-excitation. E(B-V) is calculated using the observed Balmer decrement for each spaxel when both H $\alpha$  and H $\beta$  are well determined (i.e.,  $> 1\sigma$ ). Dust-corrected line fluxes (see Table 3) are also used to determine the metallicity ([Curti et al. 2020](#)).

We find that the continuum emission peaks to the north of the field (Figure 5). Most of the line flux is concentrated in the three components, with the exception of the weaker [SII] $\lambda$ 6716,6731, which is strongest between components HZ10-E and HZ10-C. Due to the faintness of [SII] $\lambda$ 6716,6731, we are not able to present maps of  $n_e$ . The kinematics of [OIII] $\lambda$ 4959,5007 and the other lines are comparable: a strong east-west velocity gradient with no major trends in  $w_{80}$ . HZ10-E and HZ10-W feature red and blue asymmetry, respectively, while HZ10-C straddles a separate gradient of asymmetry.

Most of the spaxels are SF-excited, with the possible exception of a few low-S/N pixels east of HZ10-W. Most spaxels show a low E(B-V)  $\sim 0.3 - 0.5$ , with the noteworthy exception of some spaxels to



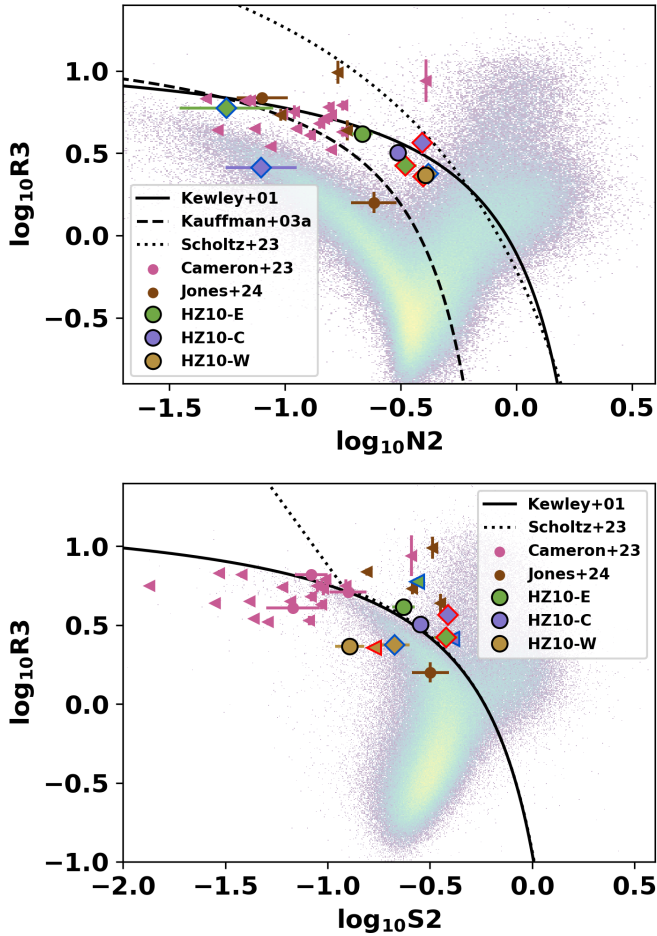


**Figure 4.** [NII]-BPT (upper) and [SII]-VO87 (lower) plots created using best-fit line fluxes for each component of HZ10, as derived from the R2700 spectra (see the values in Table 2). Best-fit narrow components, broad components, and total models for each component are shown with blue, red, and black outlines, respectively. The distributions of low-redshift galaxies from SDSS (MPA-JHU DR8 catalogue; Kauffmann et al. 2003a; Brinchmann et al. 2004) are shown as background points. Left-facing arrows represent  $3\sigma$  upper limits. We include the demarcation lines for the  $z \sim 0$  galaxies of Kewley et al. (2001, solid lines) and Kauffmann et al. (2003b, dashed line), as well as the high-redshift demarcation of Scholtz et al. (2023). We compare our results with values from  $z \sim 5.5 - 7.0$  galaxies observed with the JWST/NIRSpec MSA (Cameron et al. 2023b) as well as the  $z = 6.34 - 6.36$  galaxies in HFLS3 detected with the JWST/NIRSpec IFU (Jones et al. 2024a).

the north of HZ10-E. HZ10-E shows a low metallicity ( $\sim 0.3 - 0.5$  solar), while HZ10-C and HZ10-W are higher ( $\sim 0.5 - 0.7$  solar).

### 3.3.2 R100 resolved analysis

Next, we may follow the same spectral fitting procedure outlined in Section 3.2 to fit the line and continuum emission in spectra extracted from each spaxel of the R100 data cube. The spectrum of each spaxel is extracted from the R100 cube and is fit using LMFIT in ‘leastsq’ mode. Because these data feature a broad LSF ( $\sim 10^4 \text{ km s}^{-1}$ ), they are more suited for characterising continuum emission than line emission. Thus, we focus on the continuum emission, and only include line emission in our fits in order to reduce their bias on our recovered quantities.

The best-fit continuum power law slopes bluewards of the Balmer

break ( $\beta_{UV}$ ) are recorded if the corresponding power law normalisations are well determined (i.e.,  $> 1\sigma$ ). The Balmer break value is taken as the ratio of the rest-frame fluxes above and below the Balmer break:

$$\text{Balmer Break} = \frac{\lambda_1^+ - \lambda_1^-}{\lambda_2^+ - \lambda_2^-} \frac{\int_{\lambda_2^-}^{\lambda_2^+} F_\nu(\lambda) d\lambda}{\int_{\lambda_1^-}^{\lambda_1^+} F_\nu(\lambda) d\lambda} \quad (1)$$

where  $\lambda_1^- = 0.32 \mu\text{m}$ ,  $\lambda_1^+ = 0.35 \mu\text{m}$ ,  $\lambda_2^- = 0.39 \mu\text{m}$ ,  $\lambda_2^+ = 0.41 \mu\text{m}$ . Our definition is adapted from the spectral discontinuity index in Bruzual (1983), although they target the  $4000 \text{ \AA}$  break rather than the Balmer break. Hence our spectral bands are different, reflecting the bluer wavelength of the Balmer break, effectively around  $3700 \text{ \AA}$ .

The resulting maps (Figure 6) reveal that HZ10-W features a very red continuum  $\beta_{UV} \sim -1$ , while the rest of the field features more standard values of  $\beta_{UV} \sim -2$ . On the other hand, the Balmer break values at all three primary locations is comparable, though we notice a spatial anticorrelation between stronger breaks and stronger nebular emission lines.

## 4 DISCUSSION

### 4.1 Lack of evidence for presence of AGN

From the previous Section, it is apparent that HZ10 is a complex system, with a strong velocity gradient and asymmetric emission lines. While the emission line ratio diagnostics are not able to confirm or refute the presence of an AGN, we may use other methods to search for AGN signatures. Here, we explore whether there is a broad line region (BLR) in this system (Section 4.1.1), and if there are high-ionisation lines detected (Section 4.1.2).

#### 4.1.1 Testing for the presence of a BLR

BLRs, which represent high-dispersion gas in the immediate surroundings of an accreting black hole, have been discovered in multiple  $z > 4$  galaxies with JWST/NIRSpec through the detection of broad (FWHM  $> 10^3 \text{ km s}^{-1}$ ) components of permitted lines, typically Balmer hydrogen lines ( $H\alpha$  and  $H\beta$ ; e.g., Maiolino et al. 2024; Parlanti et al. 2024; Übler et al. 2024b; Loiacono et al. 2024). Crucially, forbidden lines (including [OIII] $\lambda\lambda 4959, 5007$ , [NII] $\lambda\lambda 6548, 6584$ , and [SII] $\lambda\lambda 6716, 6731$ ) are not emitted from BLRs due to suppression in high-density environments (e.g., Baskin & Laor 2005; Cresci et al. 2023).

In Section 3.2, we extracted spectra from the R2700 data cube using circular apertures of radius  $0.125''$  centred on each of the three line peaks, and fit each with a two-component (broad and narrow) model for each line. To allow for the presence of a BLR, we allowed the linewidths of each forbidden line to differ from the linewidths of the Balmer lines. The resulting fits (Figure 2) and best-fit values (Table 2) show that the broad component is redshifted in HZ10-E and blueshifted in HZ10-W. Both the Balmer lines and [OIII] $\lambda\lambda 4959, 5007$  feature a broad component with FWHM  $< 10^3 \text{ km s}^{-1}$ . Because there is no strong evidence for an extreme broad component (e.g., Parlanti et al. 2024; Übler et al. 2024b), it is likely that the broad component in these spectra does not originate from an extreme BLR, and instead represents a tidal feature or outflow. However, we note that a weak BLR may still be present, contributing to the broad emission.



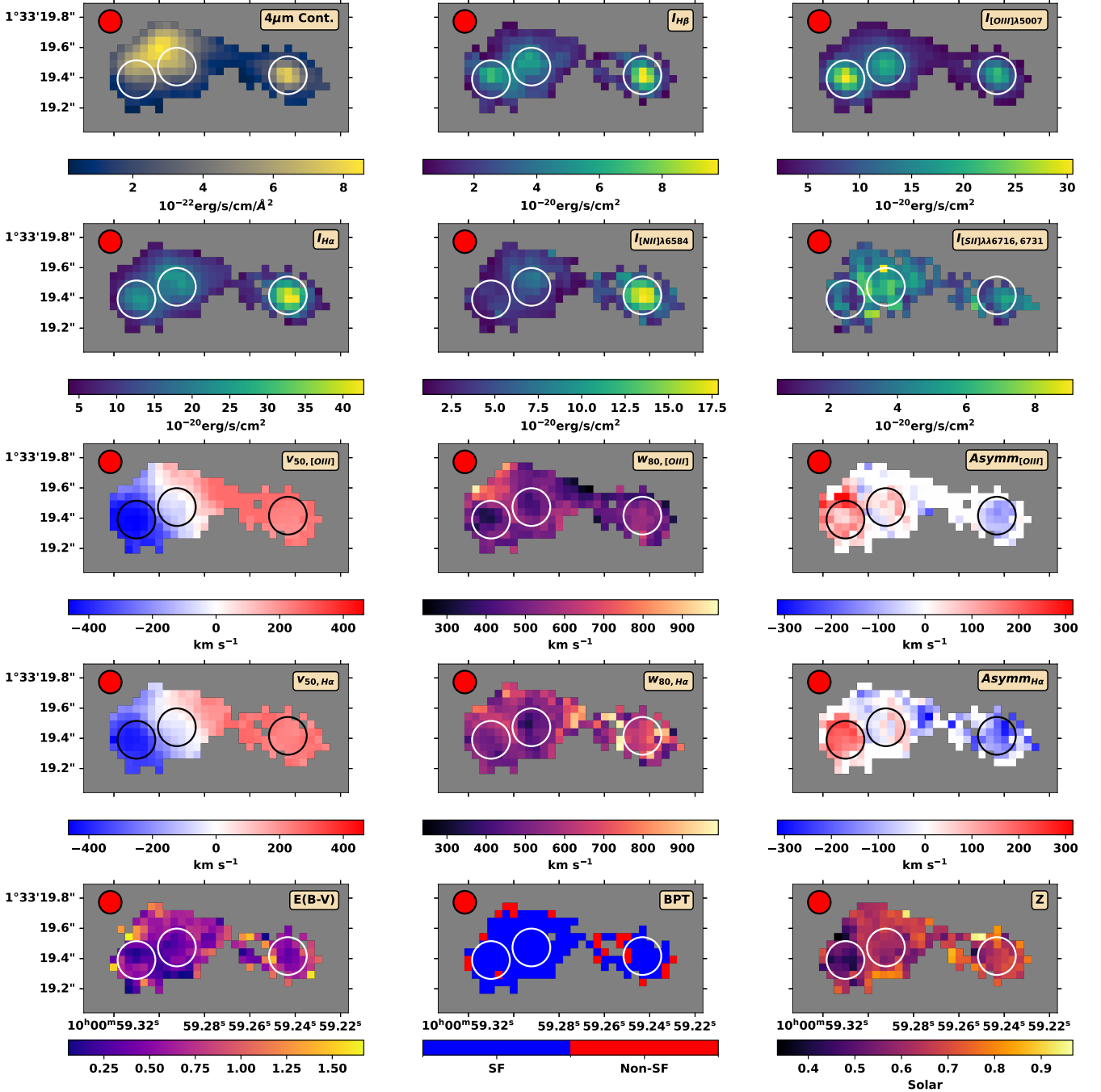


**Figure 5.** Results of fitting the spectrum of each spaxel in the R2700 data cube. We include the continuum flux at  $\lambda_{obs} = 4\ \mu\text{m}$ , integrated line intensities, and kinematic measures. In addition, we present the colour excess  $E(B-V)$ , the [NII]-BPT classification of Scholtz et al. (2023), and the gas-phase metallicity. Hollow circles depict the location of each line peak (see Figure 1), while the fiducial PSF (FWHM =  $0.15''$ ) is depicted by a red circle to the upper left.

#### 4.1.2 Lack of high-ionisation lines

We also conduct a search for high-ionisation lines (ionisation energies of  $\sim 50 - 100\ \text{eV}$ ): CIV $\lambda\lambda 1548, 1551$ , HeII $\lambda 1640$ , and [NeIV] $\lambda\lambda 2422, 2424$  (e.g., Feltre et al. 2016; Laporte et al. 2017; Nakajima et al. 2018; Maiolino et al. 2024). A detection of these lines indicates a hard ionising spectrum (e.g., Topping et al. 2024a), and they have been used to construct line ratio diagnostics that separate AGN and star-forming environments more successfully than the [NII]-BPT and [SII]-VO87 diagrams (e.g., Shirazi & Brinchmann

2012). On the other hand, non-detections have been used to argue against photoionization by an AGN (e.g., Williams et al. 2014).

We search for evidence of these lines in spectra extracted from the R100 data cube using the same component-focused apertures of Section 4.1.1. The resulting spectra are shown in Figure 7, where we also present a fit to the continuum. It is clear that none are detected at high significance. For HZ10-E, there is a range of elevated emission between CIV $\lambda\lambda 1548, 1551$  and HeII $\lambda 1640$ , but since it contains a trough, is low significance, and is similar in appearance to the noise

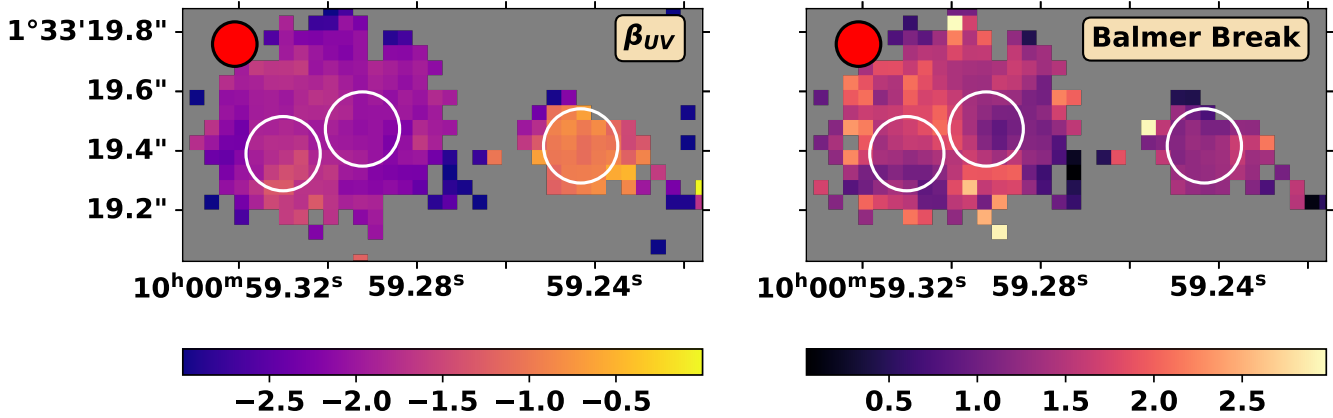


**Figure 6.** Results of fitting the spectrum of each spaxel in the R100 data cube. We include the power law slope before the Balmer break ( $\beta_{UV}$ ) and the value of the Balmer break strength. Hollow circles depict the location of each line peak (see Figure 1), while the fiducial PSF (FWHM= 0.15'') is depicted by a red circle to the upper left. The field of view is the same as in Figure 5.

artefacts common at the red end of PRISM/CLEAR spectra, it is not a strong detection.

These non-detections suggest that the three primary line-emitting components of HZ10 are not dominated by high-ionisation regions. However, we note that the spectral range required for the detection of these lines is only covered by the low spectral resolution R100 data. Higher spectral resolution observations may reveal fainter and narrower lines (e.g., Bunker et al. 2023; Maiolino et al. 2024).

#### 4.2 Comparison with ALMA [C II] Data

The JWST data presented in this work allow us to characterise the UV-bright emission of HZ10, but we are still plagued by the effects of dust extinction. This may be examined through the Balmer decrement and colour excess  $E(B-V)$  (see Figures 5 and 6), but it is still possible that there are highly attenuated areas whose faint UV emission falls beneath our sensitivity limit. To examine this possibility, we leverage high-spatial resolution ALMA data targeting [C II] emission in this field from the CRISTAL survey (Herrera-Camus et al. in prep.), which are analysed in a parallel work (Telikova et al. in prep.).

Many works have shown that [C II] is a suitable tracer of the total SFR of galaxies in the local and  $z > 4$  Universe (e.g., De Looze et al. 2014; Schaerer et al. 2020). However, recent works have argued that it is better suited as a tracer of the atomic (e.g., Vizgan et al. 2022b) or molecular gas (e.g., Zanella et al. 2018; Dessauges-Zavadsky et al. 2020; Vizgan et al. 2022a; D’Eugenio et al. 2023b; Aravena et al. 2024), and observations of low metallicity ( $\sim 0.2 - 0.7$  solar) dwarf galaxies suggest that [C II] may be a better tracer of total molecular gas content than the commonly used CO or [CI] tracers (Madden et al. 2020). This complexity arises partly from the low ionisation potential of carbon (11.26 eV), which enables [C II] emission from multiple phases of the ISM (i.e., warm and dense molecular gas, warm or cold neutral gas; e.g., Langer et al. 2010; Pineda et al. 2013; Gurman et al. 2024). In this work, we interpret [C II] as a tracer of molecular gas, but note that it is more generally a tracer of potential and/or ongoing star formation that is less affected by dust obscuration than rest-UV or rest-optical tracers.

We compare the ALMA [C II] distribution with the observed  $H\alpha$  and  $\lambda_{obs} = 4 \mu\text{m}$  continuum maps derived through spaxel-by-spaxel fits to the R2700 cube (see Section 3.3.1) in Figure 8. The astrometry of both datasets have been aligned to the Gaia DR3 system, so no

further spatial shifts are required. The restoring beam of the ALMA data (FWHM of  $0.343'' \times 0.271''$  at a position angle of  $54.6^\circ$ ) is large relative to the NIRSpec IFU PSF (FWHM  $\sim 0.1 - 0.2''$ , D’Eugenio et al. 2023a; we assume a fiducial FWHM= 0.15''), so a direct comparison is slightly ambiguous (top row of Figure 8). To better compare these data, we convolve the NIRSpec and ALMA datasets with the PSF of the other, in order to reach a common resolution (bottom row of Figure 8).

From Figure 8, it is clear that the  $H\alpha$  emission (tracing unobscured SF) largely overlaps with the [C II] emission, with the exception of a slight offset between the tracers for HZ10-W. On the other hand, the  $\lambda_{obs} = 4 \mu\text{m}$  continuum emission of the HZ10-E/HZ10-C complex is offset from the [C II] emission.

Offsets between [C II] and UV emission are commonly observed at high redshift (e.g., Maiolino et al. 2015; Inoue et al. 2016; Carniani et al. 2017, 2018; Killi et al. 2024). It has been suggested that these offsets may be caused by a non-isotropic dust distribution, as [C II] may be observed from dusty regions of the cold neutral medium (e.g., Katz et al. 2017). With this in mind, the relative distribution of  $H\alpha$ , [C II], and UV continuum flux suggests that all three line-emitting components of HZ10 feature unobscured SF (seen by the overlap between [C II] and  $H\alpha$ ), while there is a region of low molecular content but high stellar mass to the north of HZ10-C (seen by the offset between the  $\lambda_{obs} = 4 \mu\text{m}$  continuum and [C II] emission), and HZ10-W has associated obscured SF to the east (shown by the offset between the  $H\alpha$  and [C II] emission).

#### 4.3 Nature of components

In this work, we have used the R100 and R2700 data cubes to characterise the HZ10 system in both a component-based and spatially resolved manner. The line emission is concentrated in three peaks (here called HZ10-E, HZ10-C, and HZ10-W), while the continuum emission overlaps these peaks and features additional emission to the north of HZ10-C. All three components show broad [OIII] $\lambda\lambda 4959, 5007$  and Balmer lines, which imply tidal features or outflows rather than the presence of a BLR. We cannot confirm the presence of an AGN in each component, as common high-ionisation lines are not detected. Here, we synthesise our analyses to propose the natures of different parts of this field.

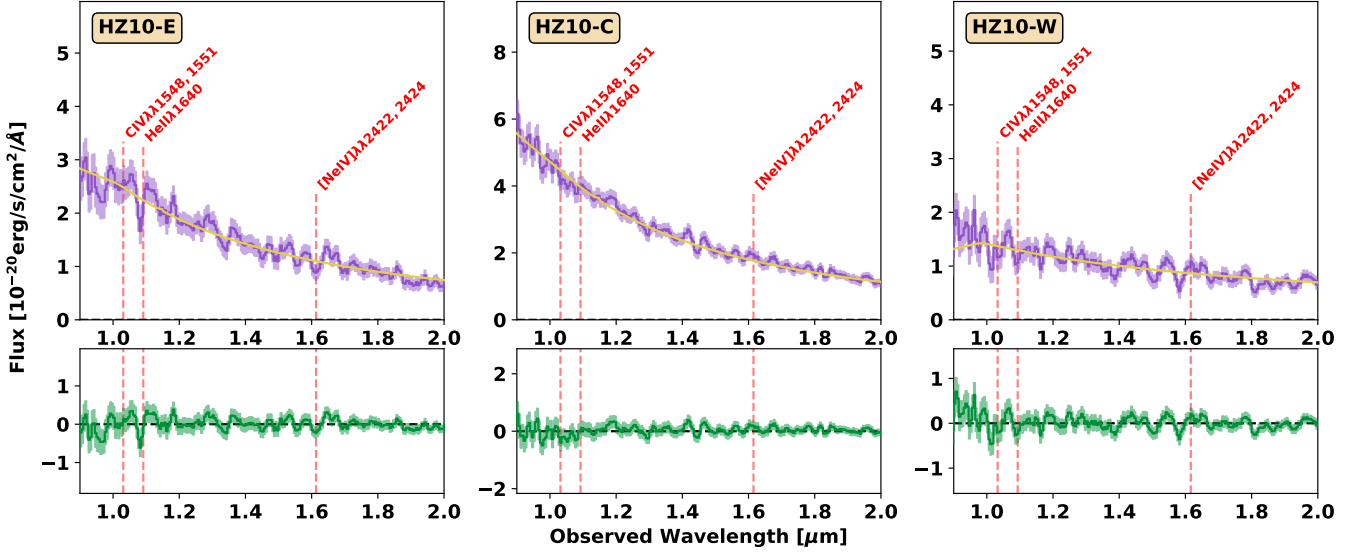


**Figure 7.** Spectra extracted from the R100 data cube, using circular apertures centred on each component, focused on three high-excitation emission lines (red vertical dashed lines). We present a fit to the continuum of each spectrum (yellow line), as well as residuals (green line).

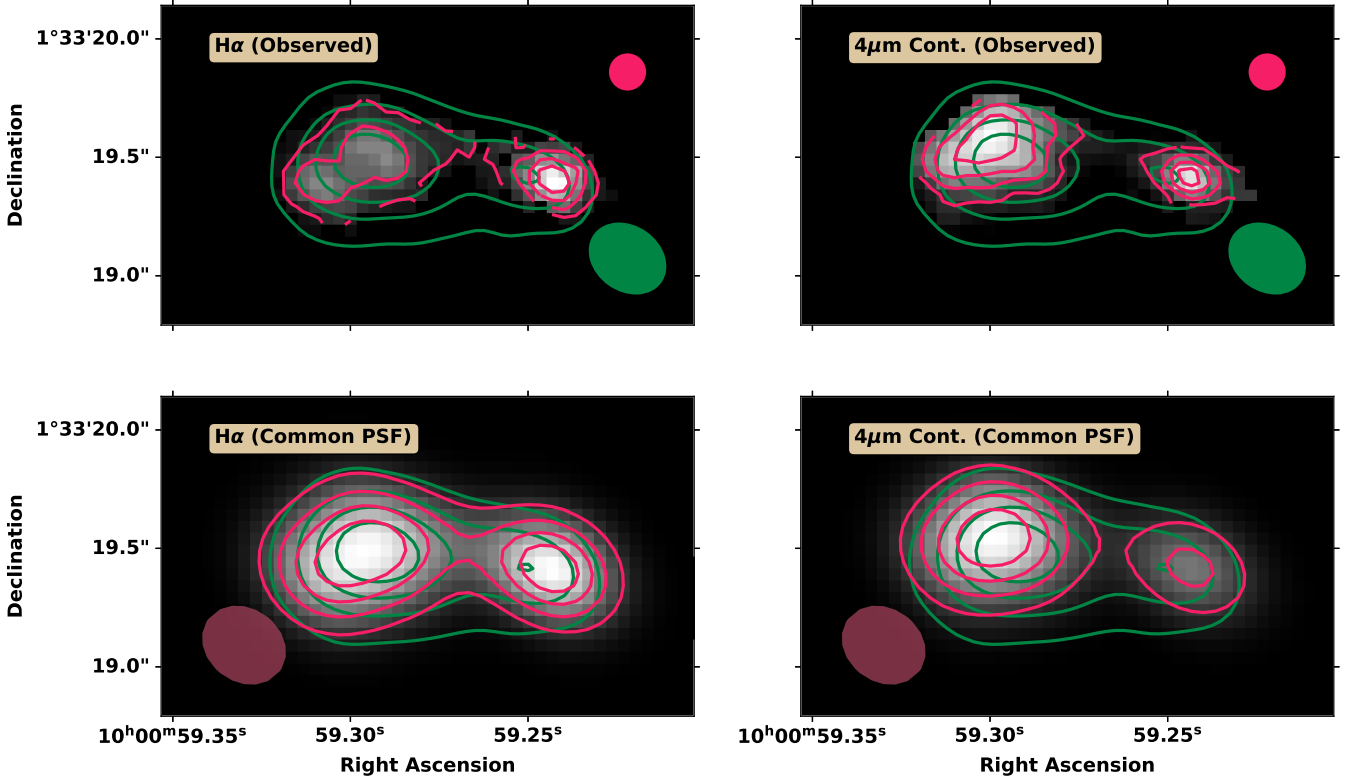


**Figure 8.** Comparison of  $H\alpha$  (pink contours and greyscale in left column) and  $\lambda_{obs} = 4\mu\text{m}$  emission (pink contours and greyscale in right column) from our JWST/NIRSpec R2700 data cube (Section 3.3.1) with ALMA  $[C\ II]$  emission (green contours in each panel; Telikova et al. in prep). The top row shows the NIRSpec data at their native resolution, while the ALMA and NIRSpec data in the lower row are convolved to the same resolution. The approximate PSFs are shown by filled ellipses.

### 4.3.1 HZ10-W

Because HZ10-W is spatially separated from the other emission, features overlapping line and continuum emission, and has a nearly uniform  $w_{80}$ , [OIII] $\lambda$ 5007 rest-frame equivalent width (see Appendix C), and metallicity, we conclude that this is an independent galaxy with a coincident stellar and gas component. Its small spatial separation ( $< 5$  kpc, projected) and line of sight velocity offset ( $< 500$  km s $^{-1}$ ) suggest that it is kinematically associated with the rest of HZ10. It also features strong blue asymmetry in all lines, which could represent previous tidal interactions or an outflow.

It is clear that HZ10-W has a red continuum ( $\beta_{UV} \gtrsim -1$ ). An in-depth analysis of JWST/NIRCam data from the JWST Advanced Deep Extragalactic Survey (JADES) revealed that the median UV spectral slope for galaxies at  $z \sim 5.9$  is  $\beta_{UV} = -2.26 \pm 0.03$  (Topping et al. 2024b). While values around  $-2$  are commonly observed (e.g., Dunlop et al. 2013; Bouwens et al. 2014), there have been cases of very red objects at high redshift (e.g.,  $\beta_{UV} \sim -1.2$  at  $z \sim 7$  in Smit et al. 2018;  $\beta_{UV} \sim -1.1$  at  $z \sim 6.5$ , Matthee et al. 2019). At a given redshift,  $\beta_{UV}$  has been found to correlate with  $M_*$ , and anti-correlate with  $M_{UV}$  (e.g., Bhatwdekar & Conselice 2021). However, the intrinsic and observed UV slopes may differ due to dust attenuation (e.g., Wilkins et al. 2013), so redder slopes may indicate larger amounts of dust. Regardless, HZ10-W features the reddest continuum slope, highest metallicity, and highest E(B-V) of the three HZ10 line-emitting components (Table 4), implying a more enriched system than the rest of HZ10.

### 4.3.2 HZ10-E and HZ10-C

HZ10-E and HZ10-C are more complex, as they feature a velocity gradient, independent areas of low  $w_{80}$ , and separate peaks of line emission. If they represented a single regular rotating disk, then we would expect to see coincident peaks of line and continuum emission in the centre of a symmetric velocity gradient. Since the peaks are offset from the centre<sup>3</sup>, this likely instead represents a pair of galaxies. HZ10-E also exhibits a redder  $\beta_{UV}$ , higher E(B-V), and lower metallicity than HZ10-C, arguing in favour of two distinct galaxies.

From comparison between the line and continuum emission (Fig. 1), it is clear that these two line peaks are not the only populations in the emission complex. The region to the northeast of these line peaks is UV-luminous but faint in line emission, suggesting a gas-poor population of stars that may be seen immediately post-starburst ( $\sim 10$  Myr). Further evidence for this is given by a comparison of the JWST data to new ALMA [C II] data, which shows that this northeast region is not [C II]-luminous (i.e., low  $M_{H_2}$ ). It is true that this region does not show drastic signs of difference in the gas-phase diagnostics (e.g.,  $\beta_{UV}$ ,  $Z$ , E(B-V)), but this may signify that these diagnostics are dominated by gas stripped from HZ10-E and HZ10-C. This also argues against the idea that the northeast emission represents a low-redshift interloper.

### 4.3.3 Other components

Curiously, HZ10-E features red asymmetry, while HZ10-C straddles a red/blue asymmetry gradient. The blue portion is between HZ10-E

and HZ10-C, where  $w_{80}$  is larger. Because of the close separation between these two line peaks, they may simply be due to coincident emission from HZ10-E and HZ10-C, rather than a physical feature (e.g., a shock). Indeed, inspection of the R2700 data cube shows two separate intensity peaks for [OIII] $\lambda$ 5007 in these intermediate spaxels (i.e., originating from HZ10-E and HZ10-C), rather than a single peak with an extended wing. On the other hand, this interpretation does not explain the regions with blue asymmetry to the west and northeast of HZ10-C. These may represent tidal interactions, outflows, or satellite gas clumps of the merging system.

### 4.3.4 Summary

Together, these findings suggest that the eastern emission in HZ10 is composed of three primary constituents: two star-forming galaxies with redshifted broad components (HZ10-E and HZ10-C) and a gas-poor stellar component to the north. The western emission (HZ10-W) features blueshifted broad components and coincident UV and line emission. Due to the proximity of these sources, this complex picture suggests an ongoing merger of multiple galaxies.

In order to classify ‘close’ pairs of galaxies, it is common to apply the criteria of  $\Delta r \lesssim 20$  kpc and  $\Delta v \lesssim 500$  km s $^{-1}$  (e.g. Duncan et al. 2019; Ventou et al. 2019; Romano et al. 2021). All of the components in HZ10 meet the spatial separation criterion ( $< 5$  projected kpc), and the neighbouring components (i.e., HZ10-E/HZ10-C and HZ10-C/HZ10-W) meet the line-of-sight velocity criterion. Thus, it is likely that all three line-emitting galaxies will merge.

Simulations have shown that major mergers may result in multiple clumps of gas within  $\sim 5$  kpc (e.g., Kohandel et al. 2019; Rizzo et al. 2022), while observations at cosmic noon ( $z \sim 2$ ) have revealed that close mergers may feature nearly continuous velocity gradients (e.g., Simons et al. 2019), as is the case here. The presence of such gas-rich and gas-poor components in the same system is odd at first glance, but similar systems have already been discovered at high redshift (e.g., Jekyll and Hyde; Schreiber et al. 2018; Pérez-González et al. 2024).

## 5 CONCLUSIONS

In this work, we present both high ( $R \sim 2700$ ) and low spectral resolution ( $R \sim 100$ ) JWST/NIRSpec IFU data of the  $z \sim 5.7$  dusty star-forming galaxy HZ10, as part of the GTO program GA-NIFS. The high spatial resolution (PSF  $\sim 0.15''$ ) of our data opens a new window into the stellar and ionised gas properties of this source, revealing multiple components within a  $\sim 1.5''$  diameter region: three components detected in emission lines (HZ10-E, HZ10-C, and HZ10-W) and an additional offset UV continuum source.

We extract spectra from the R2700 data cube using circular apertures centred on each line-emitting component and fit each with a combined continuum and line model (H $\beta$ , [OIII] $\lambda$ 4959,5007, [NII] $\lambda$ 6548,6584, H $\alpha$ , [SII] $\lambda$ 6716,6731). Each line is well fit by a two-component model, suggesting the presence of tidal features. Through line ratio analyses, we find little evidence for AGN domination ([NII]-BPT and [SII]-VO87 diagrams), a high metallicity (0.5 – 0.7 solar, using the strong line diagnostics of Curti et al. 2020), and a range of electron densities from the flux ratio of the [SII] $\lambda$ 6716,6731 doublet:  $\log_{10}(n_e/cm^{-3}) = 2.5 - 3.1$ . The R100 spectrum (which features a wider wavelength range) also exhibits emission from the unresolved doublet [OII] $\lambda$ 3726,3729, a range of UV spectral slopes ( $\beta_{UV} \sim -2.0$  to  $-1.0$ ), and no significant Ly $\alpha$

<sup>3</sup> We note that two distinct peaks could also arise in a disc with a more dust-obscured centre. While this scenario is not implausible in and of itself, in our case there is no evidence of high obscuration in the spatial region between the two emission peaks, ruling out this scenario.



emission (with an upper limit in agreement with a previous detection, see Appendix B).

The great potential of the IFU data is exploited by then exploring each cube on a spaxel-by-spaxel basis. Line emission is focused in the three primary components, while continuum emission ( $\lambda_{obs} = 4 \mu\text{m}$ , or  $\lambda_{rest} \sim 0.60 \mu\text{m}$ ) features an extension to the north. A significant east-west velocity gradient is detected. HZ10-E and HZ10-C show red line asymmetries, while HZ10-W features blue asymmetry. No major trends in metallicity or E(B-V) are detected, while HZ10-W is found to exhibit a red spectral slope  $\beta_{UV} \sim -1$ .

We find that since all of the lines (i.e., both Balmer and forbidden lines) features both a narrow and broad component with  $\text{FWHM} < 10^3 \text{ km s}^{-1}$ , there is little evidence for a strong BLR. In the same regions, we do not significantly detect high-ionisation lines that would indicate AGN photoionisation. Thus, the asymmetric line profiles in the current data indicate the presence of outflows, tidal tails, and/or minor satellites. Further observations at higher spectral resolution are required to confirm this.

Through a comparison to new high-resolution ALMA [C II] data (Telikova et al. in prep), we find that the H $\alpha$  and [C II] emission are nearly spatially aligned, indicating ongoing star formation from molecular gas reservoirs. On the other hand, the rest-UV continuum emission to the north of HZ10-C is offset from the [C II], suggesting a gas-poor population.

Together, our analyses suggest a re-interpretation of the well-studied source HZ10. While previous observations at low spatial resolution suggested a galaxy with a strong rotation gradient and offsets between some tracers, we are now able to resolve multiple separate galaxies. Due to their close spatial and spectral association, they likely represent a merging group. One galaxy is spatially separated, features nearly coincident UV continuum, [C II], and line emission (HZ10-W), and has a blue line asymmetry. To the east of this object lies a complex group of two line emitting peaks (HZ10-E and HZ10-C) with a strong velocity gradient and red line asymmetry. Furthermore, there is a UV-bright population of gas-poor stars to the north of these galaxies which may represent a separate galaxy or a distinct region of HZ10-C.

The analysis presented here represents a major step forward in the characterisation of the ionised gas morpho-kinematics, ISM conditions, and general nature of a FIR-bright, high-redshift group of galaxies. There are still some ambiguities, which may be remedied by higher spectral resolution NIRSpec/IFU observations in different gratings (e.g., G140H). Future SED analysis of the R100 data presented in this work will result in new estimates on stellar mass and star formation history. Work is already underway on ALMA high-resolution [C II] (Telikova et al. in prep) and FIR-emitting dust analyses (Villanueva et al. in prep). When complete, this field will act as a key prototypical close-separation merger at high-redshift for studies of galaxy evolution.

## ACKNOWLEDGEMENTS

GCJ and AJB acknowledge funding from the ‘‘FirstGalaxies’’ Advanced Grant from the European Research Council (ERC) under the European Union’s Horizon 2020 research and innovation programme (Grant agreement No. 789056). KT was supported by ALMA-ANID grant number 31220026. KT, MA, and RHC acknowledge support from the ANID BASAL project FB210003. SA, MP, and BRdP acknowledge grant PID2021-127718NB-I00 funded by the Spanish Ministry of Science and Innovation/State Agency of Research (MICIN/AEI/ 10.13039/501100011033). SCa acknowledges support

from the European Union (ERC, WINGS,101040227). FDE and RM acknowledge support by the Science and Technology Facilities Council (STFC), by the ERC through Advanced Grant 695671 ‘‘QUENCH’’, and by the UKRI Frontier Research grant RISEandFALL. HÜ gratefully acknowledges support by the Isaac Newton Trust and by the Kavli Foundation through a Newton-Kavli Junior Fellowship. GC acknowledges the support of the INAF Large Grant 2022 ‘‘The metal circle: a new sharp view of the baryon cycle up to Cosmic Dawn with the latest generation IFU facilities’’. RHC thanks the Max Planck Society for support under the Partner Group project ‘‘The Baryon Cycle in Galaxies’’ between the Max Planck for Extraterrestrial Physics and the Universidad de Concepción. IL acknowledges support from PID2022-140483NB-C22 funded by AEI 10.13039/501100011033 and BDC 20221289 funded by MCIN by the Recovery, Transformation and Resilience Plan from the Spanish State, and by NextGenerationEU from the European Union through the Recovery and Resilience Facility. PGP-G acknowledges support from grant PID2022-139567NB-I00 funded by Spanish Ministerio de Ciencia e Innovación MCIN/AEI/10.13039/501100011033, FEDER *Una manera de hacer Europa*. VV acknowledges support from the ALMA-ANID Postdoctoral Fellowship under the award ASTRO21-0062. GCJ would like to thank Elena Bertola, Jorge González-López, Cosimo Marconcini, and Aayush Saxena for useful discussion and feedback on the manuscript.

## DATA AVAILABILITY

The NIRSpec data used in this research has been obtained within the NIRSpec-IFU GTO programme GA-NIFS (PID 1217) and will become publicly available May 22, 2024. Data presented in this work will be shared upon reasonable request to the corresponding author.

## REFERENCES

- Allen M. G., Groves B. A., Dopita M. A., Sutherland R. S., Kewley L. J., 2008, *ApJS*, **178**, 20
- Aravena M., et al., 2024, *A&A*, **682**, A24
- Arribas S., et al., 2023, *arXiv e-prints*, p. [arXiv:2312.00899](https://arxiv.org/abs/2312.00899)
- Asplund M., Grevesse N., Sauval A. J., Scott P., 2009, *ARA&A*, **47**, 481
- Baldwin J. A., Phillips M. M., Terlevich R., 1981, *PASP*, **93**, 5
- Baskin A., Laor A., 2005, *MNRAS*, **358**, 1043
- Bhatawdekar R., Conselice C. J., 2021, *ApJ*, **909**, 144
- Bischetti M., et al., 2018, *A&A*, **617**, A82
- Böker T., et al., 2022, *A&A*, **661**, A82
- Bouwens R. J., et al., 2014, *ApJ*, **793**, 115
- Brinchmann J., Charlot S., White S. D. M., Tremonti C., Kauffmann G., Heckman T., Brinkmann J., 2004, *MNRAS*, **351**, 1151
- Bruzual A. G., 1983, *ApJ*, **273**, 105
- Bunker A. J., et al., 2023, *A&A*, **677**, A88
- Calzetti D., Armus L., Bohlin R. C., Kinney A. L., Koornneef J., Storchi-Bergmann T., 2000, *ApJ*, **533**, 682
- Cameron A. J., Katz H., Witten C., Saxena A., Laporte N., Bunker A. J., 2023a, *arXiv e-prints*, p. [arXiv:2311.02051](https://arxiv.org/abs/2311.02051)
- Cameron A. J., et al., 2023b, *A&A*, **677**, A115
- Capak P. L., et al., 2015, *Nature*, **522**, 455
- Carilli C. L., Riechers D., Walter F., Maiolino R., Wagg J., Lentati L., McMahon R., Wolfe A., 2013, *ApJ*, **763**, 120
- Carniani S., et al., 2017, *A&A*, **605**, A42
- Carniani S., et al., 2018, *MNRAS*, **478**, 1170
- Cresci G., et al., 2023, *A&A*, **672**, A128
- Curti M., Mannucci F., Cresci G., Maiolino R., 2020, *MNRAS*, **491**, 944
- Curti M., et al., 2024, *A&A*, **684**, A75
- D’Eugenio F., et al., 2023a, *arXiv e-prints*, p. [arXiv:2308.06317](https://arxiv.org/abs/2308.06317)

- D'Eugenio C., Daddi E., Liu D., Gobat R., 2023b, *A&A*, **678**, L9
- D'Eugenio F., et al., 2024, *arXiv e-prints*, p. [arXiv:2404.06531](https://arxiv.org/abs/2404.06531)
- Davies R. L., et al., 2021, *ApJ*, **909**, 78
- De Looze I., et al., 2014, *A&A*, **568**, A62
- Delgado-Serrano R., Hammer F., Yang Y. B., Puech M., Flores H., Rodrigues M., 2010, *A&A*, **509**, A78
- Della Bruna L., et al., 2020, *A&A*, **635**, A134
- Dessauges-Zavadsky M., et al., 2020, *A&A*, **643**, A5
- Dimitrijević M. S., Popović L. Č., Kovačević J., Dačić M., Ilić D., 2007, *MNRAS*, **374**, 1181
- Dojčinović I., Kovačević-Dojčinović J., Popović L. Č., 2023, *Advances in Space Research*, **71**, 1219
- Domínguez A., et al., 2013, *ApJ*, **763**, 145
- Dors O. L., Cardaci M. V., Hägele G. F., Ilha G. S., Oliveira C. B., Riffel R. A., Riffel R., Krabbe A. C., 2024, *MNRAS*, **527**, 8193
- Duncan K., et al., 2019, *ApJ*, **876**, 110
- Dunlop J. S., et al., 2013, *MNRAS*, **432**, 3520
- Feltre A., Charlot S., Gutkin J., 2016, *MNRAS*, **456**, 3354
- Ferreira L., Conselice C. J., Duncan K., Cheng T.-Y., Griffiths A., Whitney A., 2020, *ApJ*, **895**, 115
- Fluetsch A., et al., 2021, *MNRAS*, **505**, 5753
- Fraternali F., Karim A., Magnelli B., Gómez-Guijarro C., Jiménez-Andrade E. F., Poses A. C., 2021, *A&A*, **647**, A194
- Gaia Collaboration et al., 2016, *A&A*, **595**, A1
- Gaia Collaboration et al., 2021, *A&A*, **649**, A1
- Garman A., Hu C.-Y., Sternberg A., van Dishoeck E. F., 2024, *ApJ*, **965**, 179
- Hashimoto T., et al., 2023, *ApJ*, **955**, L2
- Heintz K. E., et al., 2023, *arXiv e-prints*, p. [arXiv:2306.00647](https://arxiv.org/abs/2306.00647)
- Herrera-Camus R., et al., 2022, *A&A*, **665**, L8
- Hervella Seoane K., Ramos Almeida C., Acosta-Pulido J. A., Speranza G., Tadhunter C. N., Bessiere P. S., 2023, *A&A*, **680**, A71
- Holt J., Tadhunter C. N., Morganti R., Emons B. H. C., 2011, *MNRAS*, **410**, 1527
- Ibar E., et al., 2015, *MNRAS*, **449**, 2498
- Inoue A. K., et al., 2016, *Science*, **352**, 1559
- Isobe Y., Ouchi M., Nakajima K., Harikane Y., Ono Y., Xu Y., Zhang Y., Umeda H., 2023, *ApJ*, **956**, 139
- Jakobsen P., et al., 2022, *A&A*, **661**, A80
- Ji X., et al., 2024, *arXiv e-prints*, p. [arXiv:2404.04148](https://arxiv.org/abs/2404.04148)
- Jones G. C., et al., 2017, *ApJ*, **850**, 180
- Jones G. C., et al., 2021, *MNRAS*, **507**, 3540
- Jones G. C., et al., 2024a, *A&A*, **682**, A122
- Jones G. C., et al., 2024b, *A&A*, **683**, A238
- Katz H., Kimm T., Sijacki D., Haehnelt M. G., 2017, *MNRAS*, **468**, 4831
- Kauffmann G., et al., 2003a, *MNRAS*, **341**, 33
- Kauffmann G., et al., 2003b, *MNRAS*, **346**, 1055
- Kennicutt Robert C. J., 1998, *ApJ*, **498**, 541
- Kewley L. J., Dopita M. A., Sutherland R. S., Heisler C. A., Trevena J., 2001, *ApJ*, **556**, 121
- Killi M., et al., 2024, *arXiv e-prints*, p. [arXiv:2402.07982](https://arxiv.org/abs/2402.07982)
- Kohandel M., Pallottini A., Ferrara A., Zanella A., Behrens C., Carniani S., Gallerani S., Vallini L., 2019, *MNRAS*, **487**, 3007
- Kretschmer M., Dekel A., Teyssier R., 2022, *MNRAS*, **510**, 3266
- Kuhn V., Guo Y., Martin A., Bayless J., Gates E., Puleo A., 2023, *arXiv e-prints*, p. [arXiv:2312.12389](https://arxiv.org/abs/2312.12389)
- Laigle C., et al., 2016, *ApJS*, **224**, 24
- Langer W. D., Velusamy T., Pineda J. L., Goldsmith P. F., Li D., Yorke H. W., 2010, *A&A*, **521**, L17
- Laporte N., Nakajima K., Ellis R. S., Zitrin A., Stark D. P., Mainali R., Roberts-Borsani G. W., 2017, *ApJ*, **851**, 40
- Le Fèvre O., et al., 2020, *A&A*, **643**, A1
- Le Tiran L., Lehnert M. D., van Driel W., Nesvadba N. P. H., Di Matteo P., 2011, *A&A*, **534**, L4
- Lelli F., Di Teodoro E. M., Fraternali F., Man A. W. S., Zhang Z.-Y., De Breuck C., Davis T. A., Maiolino R., 2021, *Science*, **371**, 713
- Loiacono F., et al., 2024, *A&A*, **685**, A121
- Madden S. C., et al., 2020, *A&A*, **643**, A141
- Maiolino R., et al., 2015, *MNRAS*, **452**, 54
- Maiolino R., et al., 2023, *arXiv e-prints*, p. [arXiv:2308.01230](https://arxiv.org/abs/2308.01230)
- Maiolino R., et al., 2024, *Nature*, **627**, 59
- Markov V., Carniani S., Vallini L., Ferrara A., Pallottini A., Maiolino R., Gallerani S., Pentericci L., 2022, *A&A*, **663**, A172
- Marshall M. A., et al., 2023, *A&A*, **678**, A191
- Matthee J., et al., 2019, *ApJ*, **881**, 124
- Mazzilli Ciraulo B., Melchior A.-L., Maschmann D., Katkov I. Y., Halle A., Combes F., Gelfand J. D., Al Yazeedi A., 2021, *A&A*, **653**, A47
- Mingozzi M., et al., 2019, *A&A*, **622**, A146
- Murayama T., et al., 2007, *ApJS*, **172**, 523
- Nakajima K., Maiolino R., 2022, *MNRAS*, **513**, 5134
- Nakajima K., et al., 2018, *A&A*, **612**, A94
- Napolitano L., et al., 2024, *arXiv e-prints*, p. [arXiv:2402.11220](https://arxiv.org/abs/2402.11220)
- Neeleman M., Prochaska J. X., Kanekar N., Rafelski M., 2020, *Nature*, **581**, 269
- Newville M., Stensitzki T., Allen D. B., Ingarciola A., 2014, LMFIT: Non-Linear Least-Square Minimization and Curve-Fitting for Python, [doi:10.5281/zenodo.11813](https://doi.org/10.5281/zenodo.11813)
- Nguyen N. H., Lira P., Trakhtenbrot B., Netzer H., Ciccone C., Maiolino R., Shemmer O., 2020, *ApJ*, **895**, 74
- Osterbrock D. E., 1989, *Astrophysics of gaseous nebulae and active galactic nuclei*
- Pallottini A., Ferrara A., Gallerani S., Vallini L., Maiolino R., Salvadori S., 2017, *MNRAS*, **465**, 2540
- Parlanti E., et al., 2024, *A&A*, **684**, A24
- Pavesi R., et al., 2016, *ApJ*, **832**, 151
- Pavesi R., et al., 2018, *ApJ*, **861**, 43
- Pavesi R., Riechers D. A., Faisst A. L., Stacey G. J., Capak P. L., 2019, *ApJ*, **882**, 168
- Pérez-González P. G., et al., 2024, *arXiv e-prints*, p. [arXiv:2405.03744](https://arxiv.org/abs/2405.03744)
- Perna M., Lanzuisi G., Brusa M., Cresci G., Mignoli M., 2017, *A&A*, **606**, A96
- Perna M., et al., 2020, *A&A*, **643**, A139
- Perna M., et al., 2023a, *arXiv e-prints*, p. [arXiv:2310.03067](https://arxiv.org/abs/2310.03067)
- Perna M., et al., 2023b, *A&A*, **679**, A89
- Pineda J. L., Langer W. D., Velusamy T., Goldsmith P. F., 2013, *A&A*, **554**, A103
- Popesso P., et al., 2023, *MNRAS*, **519**, 1526
- Poses A. C., et al., 2023, *A&A*, **669**, A46
- Proxauf B., Öttl S., Kimeswenger S., 2014, *A&A*, **561**, A10
- Richings A. J., Faucher-Giguère C.-A., Stern J., 2021, *MNRAS*, **503**, 1568
- Rizzo F., Vegetti S., Powell D., Fraternali F., McKean J. P., Stacey H. R., White S. D. M., 2020, *Nature*, **584**, 201
- Rizzo F., Kohandel M., Pallottini A., Zanella A., Ferrara A., Vallini L., Toft S., 2022, *A&A*, **667**, A5
- Rodrigues M., Hammer F., Flores H., Puech M., Athanassoula E., 2017, *MNRAS*, **465**, 1157
- Rodríguez Del Pino B., et al., 2024, *A&A*, **684**, A187
- Roman-Oliveira F., Fraternali F., Rizzo F., 2023, *MNRAS*, **521**, 1045
- Romano M., et al., 2021, *A&A*, **653**, A111
- Salpeter E. E., 1955, *ApJ*, **121**, 161
- Schaerer D., et al., 2020, *A&A*, **643**, A3
- Scholtz J., et al., 2023, *arXiv e-prints*, p. [arXiv:2311.18731](https://arxiv.org/abs/2311.18731)
- Schreiber C., et al., 2018, *A&A*, **611**, A22
- Scoville N., et al., 2007, *ApJS*, **172**, 1
- Shirazi M., Brinchmann J., 2012, *MNRAS*, **421**, 1043
- Simons R. C., et al., 2019, *ApJ*, **874**, 59
- Smit R., et al., 2018, *Nature*, **553**, 178
- Speagle J. S., Steinhardt C. L., Capak P. L., Silverman J. D., 2014, *ApJS*, **214**, 15
- Sugahara Y., et al., 2021, *ApJ*, **923**, 5
- Topping M. W., et al., 2024b, *MNRAS*,
- Topping M. W., et al., 2024a, *MNRAS*,
- Übler H., et al., 2023, *A&A*, **677**, A145
- Übler H., et al., 2024a, *arXiv e-prints*, p. [arXiv:2403.03192](https://arxiv.org/abs/2403.03192)
- Übler H., et al., 2024b, *MNRAS*, **531**, 355
- Umeda H., Ouchi M., Nakajima K., Harikane Y., Ono Y., Xu Y., Isobe Y., Zhang Y., 2023, *arXiv e-prints*, p. [arXiv:2306.00487](https://arxiv.org/abs/2306.00487)

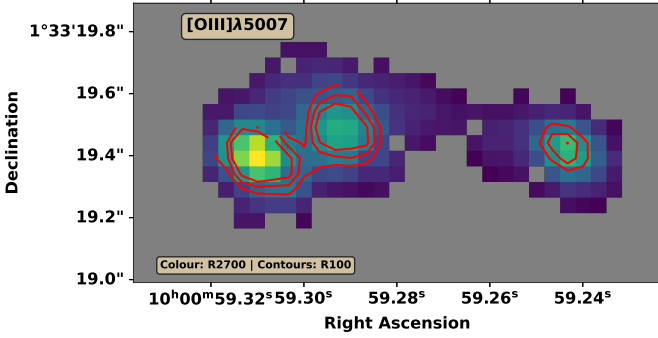


**Figure A1.** Comparison of [OIII] $\lambda$ 5007 integrated maps made from the R100 (red contours) and R2700 cubes (background colour).

Veilleux S., Osterbrock D. E., 1987, *ApJS*, 63, 295  
 Ventou E., et al., 2019, *A&A*, 631, A87  
 Venturi G., et al., 2024, *arXiv e-prints*, p. arXiv:2403.03977  
 Vieira D., Riechers D. A., Pavesi R., Faisst A. L., Schinnerer E., Scoville N. Z., Stacey G. J., 2022, *ApJ*, 925, 174  
 Vizgan D., et al., 2022a, *ApJ*, 929, 92  
 Vizgan D., Heintz K. E., Greve T. R., Narayanan D., Davé R., Olsen K. P., Popping G., Watson D., 2022b, *ApJ*, 939, L1  
 Wilkins S. M., Bunker A., Coulton W., Croft R., di Matteo T., Khandai N., Feng Y., 2013, *MNRAS*, 430, 2885  
 Williams R. J., et al., 2014, *MNRAS*, 439, 2096  
 Zanella A., et al., 2018, *MNRAS*, 481, 1976  
 de Graaff A., et al., 2024, *A&A*, 684, A87

## APPENDIX A: R100/R2700 ASTROMETRY

As mentioned in Section 2, we verified that the R100 data was aligned with the Gaia DR3 astrometric frame through comparisons to aligned HST images from the MAST archive. Since the R100 and R2700 data cubes were created using the same calibration pipeline, they should be aligned to the same frame.

This assumption was verified by comparing the [OIII] $\lambda$ 5007 integrated intensity maps of each cube. As seen in Figure A1, the two maps feature three coincident peaks, and thus do not suffer from any astrometric issues (i.e., rotation, scaling, or offsets).

## APPENDIX B: INTEGRATED SPECTRAL ANALYSIS

In the main body of this work, we characterised the HZ10 field by fitting spectra extracted from the line peaks (Section 3.2) and from each spaxel (Section 3.3). Here, we fit spectra extracted from the full HZ10 system. This approach allows for direct comparison to previous results, which treated HZ10 as a single system. An integrated analysis also allows us to predict the future evolution of the HZ10 system. However, the kinematic complexity of HZ10 (i.e., asymmetric lines) dictates that this approach does not capture the full behaviour of the system. Thus, we only present selected results from this analysis.

We begin by extracting integrated spectra from the R100 data cube using a large elliptical aperture (white ellipse in Figure 1; centred on 10m00m59.27s 01°33'19.40'' with major and minor axes of 1.6'' and 1.0'', respectively) and fit the line and continuum emission. The fitting procedure is identical to that of Section 3.2, and the resulting fit is shown in Figure B1

The continuum is well-detected in the R100 spectrum, resulting in

$M_{UV} = -22.41 \pm 0.02$  and  $\beta_{UV} = -1.9 \pm 0.02$ , in agreement with previous observations (e.g., Capak et al. 2015).

We do not detect Ly $\alpha$  emission in the R100 integrated spectrum, which yields a  $3\sigma$  upper limit on the Ly $\alpha$  rest-frame equivalent width of  $REW_{Ly\alpha} < 11\text{\AA}$ . Murayama et al. 2007 detected Ly $\alpha$  with an observed-frame equivalent width of  $75 \pm 22\text{\AA}$ , which corresponds to a rest-frame value of  $11.3 \pm 3.3\text{\AA}$  (assuming  $z_{[CII]}$  from Pavesi et al. 2016). Since this previous work predicted the Ly $\alpha$  flux using a large circular aperture of diameter 3'', this slightly larger  $REW_{Ly\alpha}$  may suggest that HZ10 exhibits a Ly $\alpha$  halo (although an integration over the full IFU field of view does not return a significant Ly $\alpha$  detection). On the other hand, the assumed redshift in the previous work ( $z = 5.7$ ) is slightly larger than the true redshift of this source, and the  $REW_{Ly\alpha}$  value is based on fits to photometry. Taking into account the uncertainties, our non-detection of Ly $\alpha$  is not in disagreement with previous results, although followup observations at higher spectral resolution (e.g., JWST/NIRSpec IFU G140H/F070LP or the Multi Unit Spectroscopic Explorer [MUSE] on the Very Large Telescope [VLT]) are needed to confirm this.

## APPENDIX C: [OIII]5007 NON-PARAMETRIC KINEMATIC ANALYSIS

Throughout this work, we have modelled each line in the R2700 spectra using two Gaussians (i.e., narrow and broad). However, this simple model may underestimate the complexity of the system. To examine this, we produce non-parametric morpho-kinematic maps for the strong, spectrally distinct line [OIII] $\lambda$ 5007 and compare them to maps produced using our two-Gaussian model.

First, we isolate all data within  $\pm 1500 \text{ km s}^{-1}$  of the systemic redshift (here assumed to be  $z = 5.6527$ ) and extract spectra for each spaxel. The continuum level for each spectrum is assumed to be constant, and is derived by creating a cumulative distribution function (CDF) of the line-free data (here assumed to be all data in  $[-1500, -750] \cup [750, 1500] \text{ km s}^{-1}$ ) and fitting this with a first-order polynomial (scipy curve\_fit). If the resulting fit features a positive, well-determined slope, it is used as the continuum flux for the spaxel, which is then subtracted from the spectrum.

The resulting line-only spectra for each spaxel are then used to derive spectral CDFs, which are normalised such that their highest and lowest values are set to unity and zero, respectively. Using PYGAM, we fit each normalised CDF with a monotonically increasing spline. If the best fit to the continuum CDF has a minimum value less than 0.1, a maximum value greater than 0.9, and a pseudo- $r^2$  value greater than 0.9, we state that it is a good fit.

The fits are used to extract the integrated line flux ( $F_L$ ), continuum flux ( $S_C$ ), the rest-frame equivalent width, and relevant kinematic measures:  $v_{50}$ ,  $w_{80}$ , and  $\text{asymmetry} = |v_{50} - v_{90}| - |v_{50} - v_{10}|$  (e.g., Hervella Seoane et al. 2023). We exclude spaxels with unrealistic kinematic measures caused by low signal (i.e.,  $|v_{50}| > 700 \text{ km s}^{-1}$ ). The line and continuum fluxes are used to derive a rest-frame equivalent width. All acceptable fits are then used to create the morpho-kinematic maps shown in Figure C1.

The results of this analysis (Figure C1) are very similar to those of our two-Gaussian approach (Figure 5). The [OIII] $\lambda$ 5007 emission is peaks in three locations, the continuum emission peaks in HZ10-W and to the north of HZ10-E and HZ10-C, a smooth east-west velocity gradient is observed, and the asymmetry pattern is maintained. Since the results of this more detailed kinematic analysis agrees with the two-Gaussian model, we use the two-Gaussian model in this work.

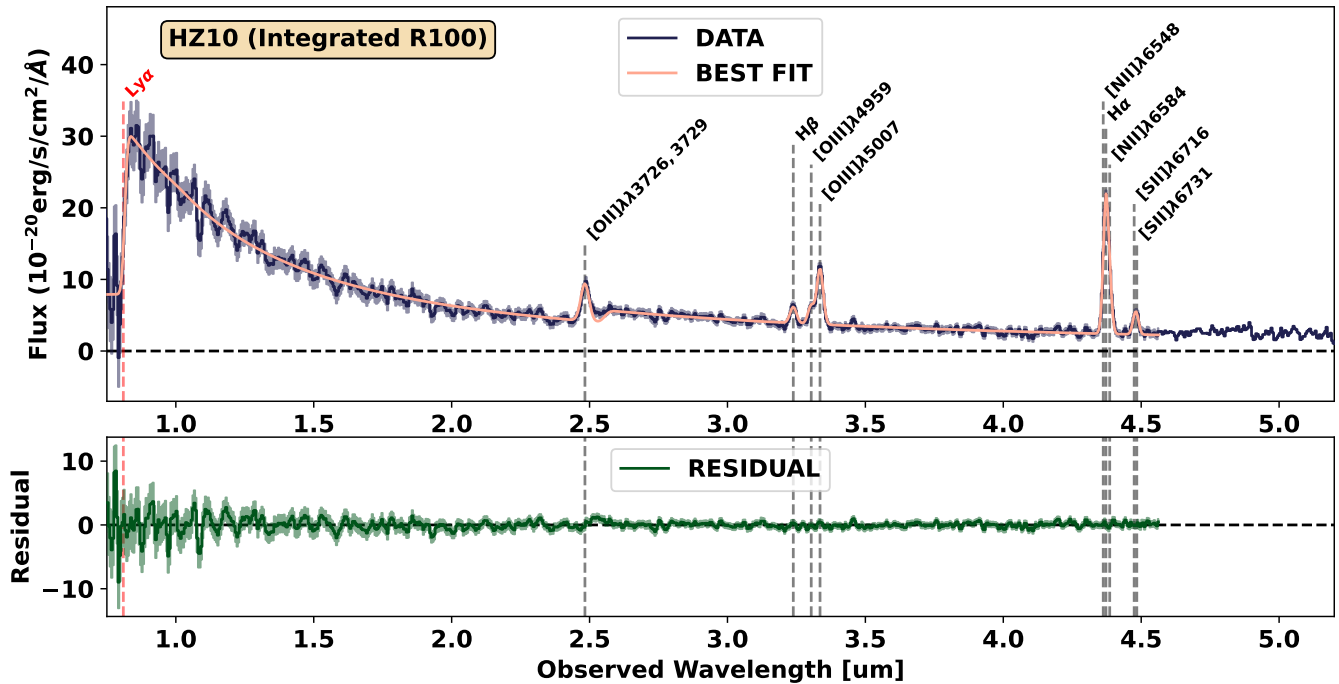


Figure B1. Integrated spectrum extracted from the R100 data cube using the elliptical aperture of Figure 1, best-fit model, and residuals.

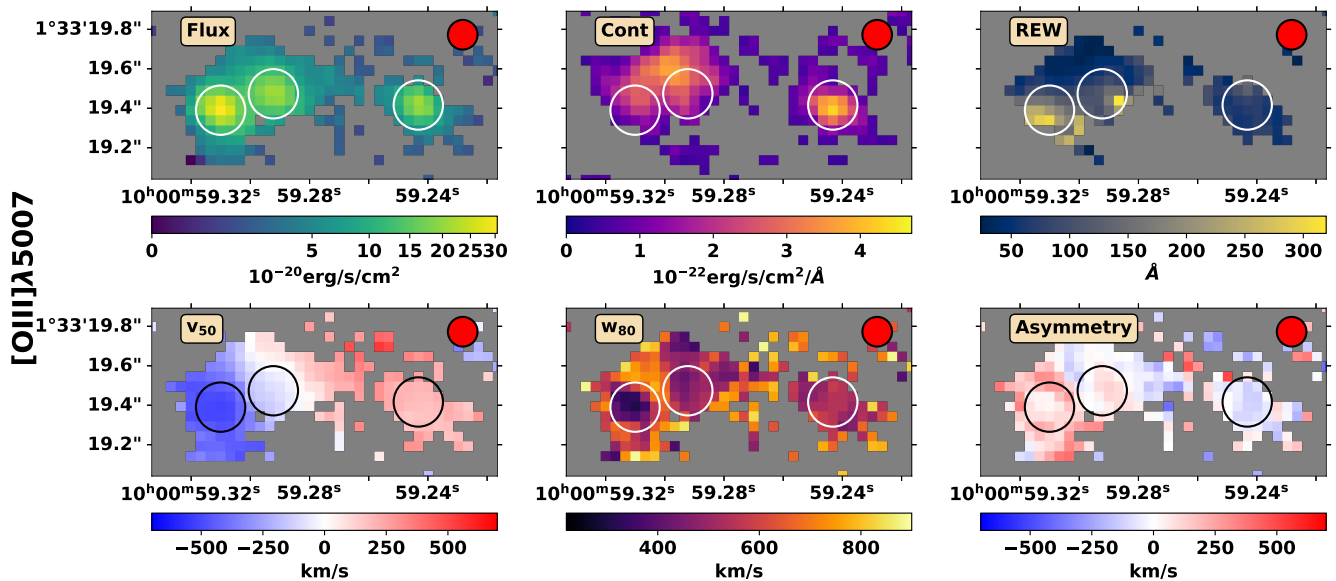


Figure C1. Morpho-kinematic maps of  $[\text{OIII}]\lambda 5007$ . We present the integrated line flux, continuum flux, rest-frame EW,  $v_{50}$ ,  $w_{80}$ , and asymmetry per spaxel. The location of each component is marked with a hollow circle, and the fiducial PSF is represented by a red ellipse to the upper right.

This paper has been typeset from a  $\text{\TeX}/\text{\LaTeX}$  file prepared by the author.